The Astrophysical Journal, 970:102 (18pp), 2024 August 1 https://doi.org/10.3847/1538-4357/ad50a5

JWST Spectroscopy of SN H0pe: Classification and Time Delays of a Triply Imaged Type Ia Supernova at $z = 1.78$

Wenlei Chen[1,2], Patrick L. Kelly[2], Brenda L. Frye[3], Justin Pierel[4], S. P. Willner[5], Massimo Pascale[6], Seth H. Cohen[7], Christopher J. Conselice[8], Michael Engesser[4], Lukas J. Furtak[10], Daniel Gilman[10,16], Norman A. Grogin[4], Simon Huber[11,12], Saurabh W. Jha[13], Joel Johansson[14], Anton M. Koekemoer[4], Conor Larison[13], Ashish K. Meena[9], Matthew R. Siebert[4], Rogier A. Windhorst[7], Haojing Yan[15], and Adi Zitrin[9]

[1] Department of Physics, Oklahoma State University, 145 Physical Sciences Building, Stillwater, OK 74078, USA; wenlei.chen@okstate.edu
[2] School of Physics and Astronomy, University of Minnesota, 116 Church Street SE, Minneapolis, MN 55455, USA
[3] Department of Astronomy/Steward Observatory, University of Arizona, 933 N. Cherry Avenue, Tucson, AZ 85721, USA
[4] Space Telescope Science Institute, 3700 San Martin Drive, Baltimore, MD 21218, USA
[5] Center for Astrophysics, Harvard & Smithsonian, 60 Garden Street, Cambridge, MA 02138, USA
[6] Department of Astronomy, University of California, 501 Campbell Hall #3411, Berkeley, CA 94720, USA
[7] School of Earth and Space Exploration, Arizona State University, Tempe, AZ 85287-1404, USA
[8] Jodrell Bank Centre for Astrophysics, Alan Turing Building, University of Manchester, Oxford Road, Manchester M13 9PL, UK
[9] Physics Department, Ben-Gurion University of the Negev, P.O. Box 653, Be'er-Sheva 8410501, Israel
[10] Department of Astronomy & Astrophysics, University of Chicago, Chicago, IL 60637, USA
[11] Max-Planck-Institut für Astrophysik, Karl-Schwarzschild-Str. 1, 85748 Garching, Germany
[12] Physik-Department, Technische Universitaet Muenchen, James-Franck-Strae 1, 85748 Garching, Germany
[13] Department of Physics and Astronomy, Rutgers The State University of New Jersey, 136 Frelinghuysen Road, Piscataway, NJ 08854, USA
[14] Oskar Klein Centre, Department of Physics, Stockholm University, AlbaNova, SE-10691 Stockholm, Sweden
[15] Department of Physics and Astronomy, University of Missouri, Columbia, MO 65211, USA

Received 2024 March 14; revised 2024 May 13; accepted 2024 May 23; published 2024 July 22

Abstract

SN H0pe is a triply imaged supernova (SN) at redshift $z = 1.78$ discovered using the James Webb Space Telescope. In order to classify the SN spectroscopically and measure the relative time delays of its three images (designated A, B, and C), we acquired NIRSpec follow-up spectroscopy spanning 0.6–5 μm. From the high signal-to-noise spectra of the two bright images B and C, we first classify the SN, whose spectra most closely match those of SN 1994D and SN 2013dy, as a Type Ia SN. We identify prominent blueshifted absorption features corresponding to Si II λ6355 and Ca II H λ3970 and K λ3935. We next measure the absolute phases of the three images from our spectra, which allow us to constrain their relative time delays. The absolute phases of the three images, determined by fitting the three spectra to Hsiao07 SN templates, are $6.5^{+2.4}_{-1.8}$ days, $24.3^{+3.9}_{-3.9}$ days, and $50.6^{+16.1}_{-15.3}$ days for the brightest to faintest images. These correspond to relative time delays between Image A and Image B and between Image B and Image C of $-122.3^{+43.7}_{-43.8}$ days and $49.3^{+12.2}_{-14.7}$ days, respectively. The SALT3-NIR model yields phases and time delays consistent with these values. After unblinding, we additionally explored the effect of using Hsiao07 template spectra for simulations through 80 days instead of 60 days past maximum, and found a small (11.5 and 1.0 days, respectively) yet statistically insignificant ($\sim 0.25\sigma$ and $\sim 0.1\sigma$) effect on the inferred image delays.

Unified Astronomy Thesaurus concepts: Type Ia supernovae (1728); Gravitational lensing (670); Strong gravitational lensing (1643); Rich galaxy clusters (2005); Spectroscopy (1558); James Webb Space Telescope (2291); Hubble constant (758)

1. Introduction

Refsdal (1964) showed that, in principle, the relative time delays between the appearances of a multiply imaged supernova (SN) could be used to constrain the Hubble constant H_0. It took more than 50 yr, however, to put this theory to use. The first strongly lensed SN with multiple resolved images, dubbed "SN Refsdal" in honor of Sjur Refsdal, was discovered in 2014 (Kelly et al. 2015, 2016), and it has been used to measure H_0 with competitive precision (Kelly et al. 2023). SN Refsdal occurred in a galaxy at $z = 1.491$ (Smith et al. 2009) and was strongly lensed by the MACS J1149.5+2223 galaxy cluster.

The method of measuring H_0 using an SN strongly lensed by a galaxy cluster involves systematic uncertainties that are different from those of measurements that instead employ quasars that are multiply imaged by galaxy-scale lenses (e.g., Suyu et al. 2017). In particular, models of galaxy-cluster lenses have substantially less sensitivity to the mass-sheet degeneracy given strongly lensed sources at multiple redshifts, and they exhibit more modest projection effects in comparison to galaxy-scale lenses. Being lensed by a galaxy cluster, SN Refsdal also had an approximately year-long time delay, which is much longer than those from galaxy-scale lenses. This enabled more precise time-delay measurements to constrain H_0.

Additional multiply imaged SNe have been found. Type Ia SN (SN Ia) iPTF16geu at $z = 0.409$ was detected in ground-

---

[16] Brinson Fellow.

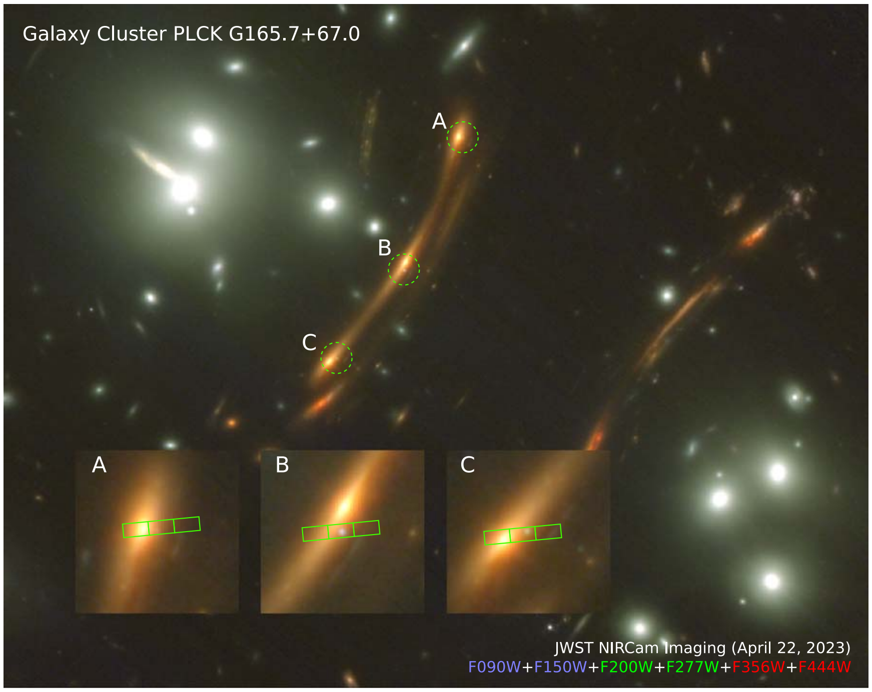

Figure 1. Color image of the Arc 2 region of G165. This "Epoch 2" NIRCam image was taken on 2023 April 22, the same day the spectra were acquired. Green dashed circles in the main image are centered on the three SN images, which are labeled A, B, and C from north to south. The three stamp images superposed on the main image show magnified images of the SN and its host galaxy with superposed green rectangles marking the open shutters in the NIRSpec micro-shutter assembly (MSA). The SN is visible as a blue point source situated at the central shutter of each slitlet. North is up and east is to the left in all images, and red represents the NIRCam F356W and F444W filters, green represents F200W and F277W, and blue represents F090W and F150W. The scale of the main image is indicated by the distance from A to C, which is 14″.

based imaging 2 yr after SN Refsdal (Goobar et al. 2017). Two other SNe, "SN Requiem" at $z = 1.95$ (Rodney et al. 2021) and "SN Zwicky" at $z = 0.354$ (Goobar et al. 2023), were identified in Hubble Space Telescope (HST) data. Recently, a multiply imaged core-collapse SN (CCSN) at $z \approx 3$ was found in archival HST images taken in 2010 (Chen et al. 2022). In addition, a candidate multiply imaged SN Ia (SN 2022riv) was detected in HST imaging (HST SNAP 16729, PI: P. Kelly) and followed up by HST and James Webb Space Telescope (JWST) observations (HST 16264, PI: J. Pierel; HST 17253, PI: P. Kelly; and JWST 2767, PI: P. Kelly), making it the first strongly lensed SN observed by JWST. However, these cases all have limitations for cosmological constraints. SN iPTF16geu and SN Zwicky are at relatively low redshifts, and the short time delays (<1 day) between the multiple images do not allow an accurate measurement of H_0 (Dhawan et al. 2020; Johansson et al. 2021). SN Requiem and the CCSN at $z \approx 3$ lack light curves for the measurement of the relative delays, and only the trailing image of SN 2022riv has been detected.

On 2023 March 30, a candidate SN Ia dubbed "SN H0pe" (Frye et al. 2023) appeared in the NIRCam images of the PLCK G165.7+67 (G165) galaxy-cluster field. SN H0pe was confirmed to be a transient when the NIRCam images were compared against HST WFC3 images taken 7 yr earlier. Follow-up spectroscopic observations using the Large Binocular Telescope (LBT) were also conducted, which yielded a precise redshift for the arc (Polletta et al. 2023). At $z = 1.78$ (Polletta et al. 2023; Frye et al. 2024), SN H0pe is the highest-redshift strongly lensed SN Ia. The candidate was followed up 23 days after discovery with NIRSpec spectroscopy and a second epoch of NIRCam imaging (Figure 1), which was followed by a third NIRCam imaging epoch 17 days later (Frye et al. 2024). SN H0pe offers the opportunity to make a second, independent measurement of H_0 using a different cluster lens.

Frye et al. (2024) described SN H0pe's discovery and a strong lensing, photometric, and spectroscopic analysis of the G165 cluster field. This paper analyses the spectroscopic data used to determine the SN's phase in each of its three images. Pierel et al. (2024) have analyzed photometry of SN H0pe in order to obtain an independent measurement of the relative time delays among the images. Pascale et al. (2024) have presented an inference of H_0 based on the time-delay measurements from these spectroscopic and photometric analyses. For this study, the spectroscopic phases were measured in a blind analysis independent of the light curve and the lens modeling. In other words, we intentionally excluded imaging data and lens models from the current analysis, and the results are based only on the NIRspec data and SN spectral templates.

The paper is organized as follows. Section 2 describes the JWST NIRSpec data set. Sections 3 and 4 presents a spectral analysis of SN H0pe and its host galaxy. Section 5 describes our methods used to measure the phases of the SN images. Section 6 outlines the simulation of our model and the error analysis. Section 7 presents the final constraints on the time delays and the magnifications of SN H0pe's images. Section 8 describes the updates after we unblinded our initial results to the H_0-inference team (Pascale et al. 2024). Section 9 discusses the implications and presents our conclusions.

2. Data

SN H0pe was detected in JWST NIRCam imaging of the galaxy cluster G165 acquired on UT 2023 March 30 by the Prime Extragalactic Areas for Reionization and Lensing

Science program (Windhorst et al. 2023; GTO 1176, PI: R. Windhorst). Frye et al. (2024) described the data reduction and analysis and the three images of the SN and its host galaxy. The SN and its host galaxy are near the central region of the galaxy-cluster field, as shown in Figure 1. SN Images A, B, and C have R.A. and decl. coordinates (J2000) 11:27:15.31, +42:28:41.0; 11:27:15.60, +42:28:33.8; and 11:27:15.94, +42:28:28.9, respectively (Frye et al. 2024, their Table 2).

We obtained follow-up JWST NIRSpec Multi-Object Spectroscopy (MOS) and NIRCam imaging on 2023 April 22 UT ("Epoch 2," DDT 4446, PI: B. Frye). The NIRSpec observations were designed using the MSA to acquire spectra of the three images of SN H0pe, two of the three images of the SN host galaxy, and 42 other gravitationally lensed arcs. The SN and host-galaxy spectra used three MSA slitlets (open shutters) end to end as shown in Figure 1. The color image was generated from the Epoch 2 NIRCam images. Each slitlet has an open area of $0\farcs20$ in the dispersion direction and $0\farcs46$ in the spatial direction. There is a $0\farcs07$ gap between slitlets, giving a total height for the three slitlets of $1\farcs52$. The NIRSpec MOS data comprised the PRISM (0.6–5.3 μm wavelength coverage at spectral resolution $R \sim 100$) and the G140M and G235M gratings (0.70–3.07 μm at $R \sim 1000$).

We began processing the spectroscopic data by downloading the Stage 2 data from the Mikulski Archive for Space Telescopes (MAST). Additional processing used the JWST pipeline[17] (Bushouse et al. 2023) with context file jwst_1087.pmap to produce two-dimensional (2D) spectral data. The pipeline applied a slit-loss throughput correction to the SN images based on their planned positions within the MSA shutters. The spectra of the SN and its host-galaxy images were extracted using the optimal extraction algorithm from Horne (1986) implemented as scripts available as part of the MOS Optimal Spectral Extraction notebook.[18] We used `webbpsf`[19] to generate the effective point-spread functions for the NIRSpec observations.

To separate the spectra of the SN and its host galaxy, we fit two kernels simultaneously to the flux in the 2D spectrum as a function of wavelength. We used a Gaussian kernel to model the flux distributions of the point source (the SN) and selected from Gaussian, Moffat (Moffat 1969), and Voigt (e.g., Whiting 1968) distribution functions to model the extended source (the host galaxy) along the spatial direction of each 2D spectrum. The kernels were chosen based on the best-fit profile functions that minimized the least-squares statistic. During the extraction process, we disregarded the uncertainties related to the kernel functions. Figure 2 shows the 2D spectrum model and the extracted spectrum for the PRISM observations of Image B. Appendix A gives complete details of the extraction method and the full complement of 2D spectra and source models for the SN. Frye et al. (2024) presented the full spectroscopic data set.

3. Spectrum of the Host Galaxy

As shown in Figure 1, the NIRSpec slitlets placed on Images A and C intersect the host galaxy's nucleus. Because the SN was faintest in Image A, the A slitlet yields the highest signal-to-noise ratio and least-contaminated spectrum of the host galaxy. Figure 3 shows the spectrum of the host, and Table 1 lists the identifications and fluxes of the detected lines. For our analysis, we used `GLEAM` (Stroe & Savu 2021), a software package that uses the `LMFIT` Python package (Newville et al. 2021) to perform the line fitting and to calculate errors on the fit parameters. The line wavelengths (excluding unresolved doublets such as [O II]) give spectroscopic redshift $z = 1.7825 \pm 0.0008$, which agrees with the spectroscopic measurement using the LBT Utility Camera in the Infrared (Polletta et al. 2023) and with an independent redshift measurement (Frye et al. 2024) from the same NIRSpec data. The line identifications also agree with Frye et al. (2024), who analyzed the spectroscopy of host-galaxy Images A and C (labeling them Arc 2a and 2c, respectively). They estimated the Hα line flux with corrections for underlying stellar absorption, dust extinction, and slit loss of the whole arc. Their Table 4 gives host-galaxy specific star formation rates (derived from the Hα flux) and stellar masses derived from Images A and C.

4. Spectra of SN H0pe

Figure 4 shows the extracted spectra of Images B and C. To classify the SN, the portions within rest wavelengths 3600 to 10000 Å were crossmatched with the SN Ia template libraries available in the Next Generation SuperFit (`NGSF`; Howell et al. 2005; Goldwasser et al. 2022) and the Supernova Identification (`SNID`; Blondin & Tonry 2007) software packages. These template libraries include all major SN types, e.g., Type I and Type II, as well as SN subtypes as defined in Blondin & Tonry (2007). For the `NGSF` analysis, the SN templates were fitted to the spectra of SN H0pe, accounting for the presence of dust extinction, while for the `SNID` analysis the observed spectra were cross-correlated with template SN spectra. The `SNID` approach, in contrast to the `NGSF` analysis, removes the continuum, and the correlation reflects the features of the spectrum as opposed to the overall shape of the spectral energy distribution.

Tables 2 and 3 list the five best-fit SN templates from `NGSF` and `SNID`, respectively. As shown in Figure 5, the SN spectra are consistent with those of an SN Ia. The spectra of Images B and C most closely match those of SN 2013dy and SN 1994D at phases of 6 days and 28 days, respectively, as indicated by the `NGSF` analysis. For the `NGSF` analysis, the favored subtype is "Ia-norm," a normal SN Ia (Blondin & Tonry 2007). Image A had the lowest signal-to-noise ratio among the three SN images, and consequently the template matching could not yield a favored SN type or subtype. If we force the match within a set of previously observed SNe Ia, the spectrum of Image A most closely matches SN 2015N at 49 days after its peak brightness. Figure 5 shows these best-match spectra superimposed on the spectra of SN H0pe for comparison. With `SNID`'s default template-matching thresholds, 176 templates—all SNe Ia—match the Image B spectrum, where 163 matching templates that are in the Ia-norm subtype. The Image C spectrum has 165 matching templates, 164 of them SNe Ia, and 107 with Ia-norm templates. No phase or even a favored SN type can be identified from the low signal-to-noise spectrum of Image A from the `SNID` analysis.

When the spectra were obtained, Image B was the brightest of the three SN images. As shown in Figure 4, the spectrum of Image B exhibits the Si II absorption feature near 6120 Å in the rest frame of the host galaxy. This is an identifying

---

[17] https://github.com/spacetelescope/jwst

[18] https://spacetelescope.github.io/jdat_notebooks/notebooks/optimal_extraction/Spectral_Extraction-static.html

[19] https://webbpsf.readthedocs.io/en/latest/index.html

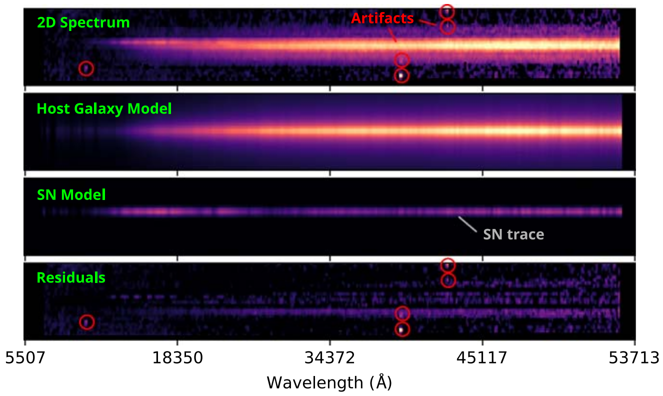

Figure 2. NIRSpec PRISM spectrum of the host galaxy and the SN from Slit B (Figure 1). Observed wavelengths are marked at the bottom, and the total height of each panel projects to 1.″52 on the sky. The top panel shows the 2D spectrum from the JWST pipeline. The middle two panels show the best-fit models of the host galaxy and the SN, respectively. The bottom panel shows the residuals after subtracting the galaxy and the SN models from the original spectrum. Red circles label the cosmic-ray-related artifacts (hot pixels) in the 2D spectrum.

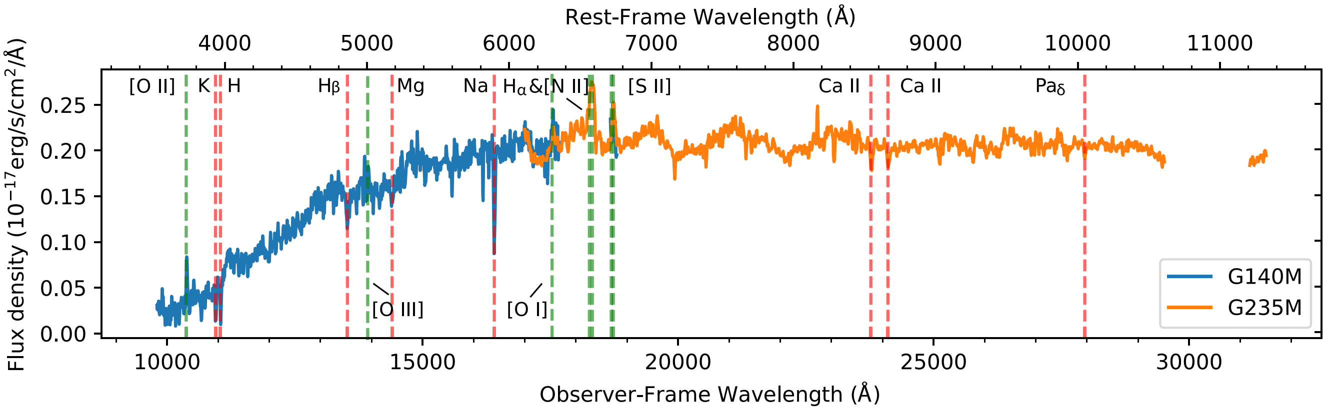

Figure 3. NIRSpec G140M and G235M spectra of the A image of the host-galaxy nucleus. The data are for the single 0.″46 slitlet containing the nucleus (Figure 1). Vertical lines mark the positions of the detected emission (green) and absorption (red) lines, as listed in Table 1. Wavelengths are marked in the observed frame (bottom) and in the $z = 1.7825$ rest frame (top). The gap in the spectrum near observed 3 μm is from the physical gap between the two NIRSpec detector chips. The spectra and line identifications for Images A and C are also shown by Frye et al. (2024).

characteristic of SN Ia spectra (Filippenko 1997): a deep absorption trough around 6150 Å produced by blueshifted Si II λ6355 emission is prominent in the spectra of SNe Ia through roughly several weeks after maximum but is absent from the spectra of other types of SNe.

Typical velocities for SNe Ia near maximum light are $v_{\rm Si\,II} \approx 10$–$12 \times 10^3$ km s^{-1} and $v_{\rm Ca\,II} \approx 13$–$15 \times 10^3$ km s^{-1} (Filippenko 1997). Figure 4 shows blueshifted Si II λ6355 and Ca II H and K (λ3935 and λ3970, respectively) absorption lines at 6117 ± 2 Å (∼17017 Å in the observer frame) and at 3790 ± 2 Å (∼10544 Å in the observer frame), respectively. These wavelengths for SN H0pe give $v_{\rm Si\,II} = -11.23 \pm 0.11 \times 10^3$ km s^{-1} and $v_{\rm Ca\,II} = -12.54 \pm 0.19 \times 10^3$ km s^{-1} relative to the host-galaxy redshift of $z = 1.7825$. From Image B, we measured an EW of the Si II λ6355 absorption lines of 56 ± 8 Å in the rest frame of the SN. Given the SN Image B phase of $6.5^{+2.4}_{-1.8}$ days (Section 5), the Si II velocity and its EW are consistent with those of a normal-velocity SN Ia or an SN 1991T-like SN Ia (e.g., Wang et al. 2013; Zhao et al. 2021).

5. Methods of Measuring Phases of the Supernova Images

We employ three methods to constrain the phases (defined as rest-frame days after peak *B*-band brightness) of the SN images. The first method is fitting the Hsiao07 (Hsiao et al. 2007) spectral templates to the NIRSpec data using Markov Chain Monte Carlo (MCMC) sampling. Hsiao et al. (2007)'s templates were constructed from a library of ∼600 spectra of ∼100 SNe Ia. The second method is similar except that the fitting instead uses the SALT3-NIR (Pierel et al. 2022) spectral SN Ia models. The original SALT3 model (Kenworthy et al. 2021) was developed from ∼1200 spectra of 380 distinct SNe Ia. To create the SALT3-NIR model, an additional 166 SNe Ia with near-infrared (NIR) data were incorporated, extending the model's reach to 2 μm. The third method is to apply the `SNID` software package[20] (Blondin & Tonry 2007), as described in Section 4. We also used `NGSF` to classify the SN spectra. However, since the default template library of `NGSF` is based on a smaller template set of SN spectra[21] selected from the WISeREP database (Yaron & Gal-Yam 2012; Goldwasser et al. 2022), the sparse temporal coverage of the SN spectral library limits our ability to infer SN phases. The details of the three analyses are described below, and Appendix B presents the constraints on the phases of the SN images from these analyses, before accounting for systematic uncertainties described in Section 6.

---

[20] The default `SNID` template library consists of 3754 spectra of 349 templates.

[21] The default `NGSF` template library includes 1004 spectra of 186 SNe.

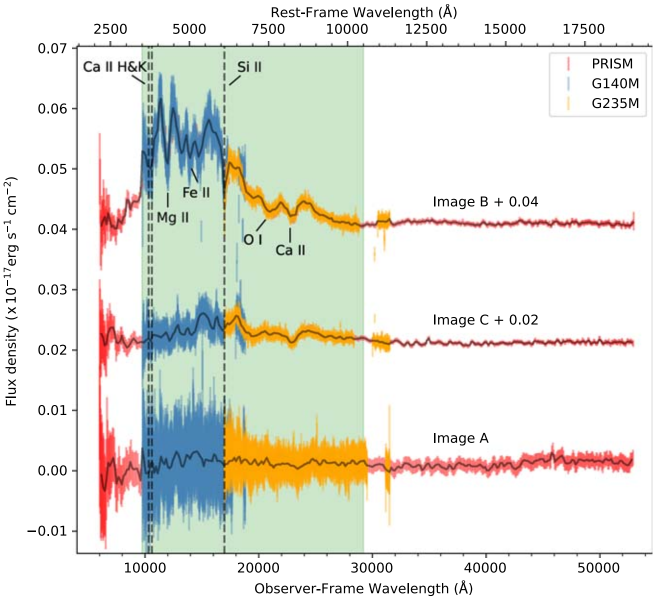

Figure 4. NIRSpec spectra of all three images of SN H0pe. Spectra are offset vertically as labeled for clarity. Error bars, merging into color bands as indicated in the legend, show the G140M, G235M, and PRISM spectra. Solid lines show the spectra rebinned to 120 Å. Wavelengths are marked in the observed frame (bottom) and the rest frame (top, based on the host-galaxy $z = 1.7825$). The green shading marks the wavelength range used to match the SN templates and measure the image phases. Dashed vertical lines mark the wavelengths of key absorption features. Spectra are plotted as extracted in a single slitlet, not corrected for slit losses.

Table 1
Emission and Absorption Lines of the A Image of the Host-galaxy Nucleus

Spectral Line	Wavelength (rest-frame Å)	Line Flux[a] ($\times 10^{-17}$ erg s^{-1} cm^{-2})	EW[b] (Å)
[O II]	3727, 3730	1.40 ± 0.22	15.6 ± 2.5
Ca K	3935	-1.13 ± 0.26[c]	-8.0 ± 1.9
Ca H	3970	-1.86 ± 0.40	-10.5 ± 2.3
Hβ	4863	-2.09 ± 0.32	-4.9 ± 0.7
[O III]	5008	0.75 ± 0.23	1.7 ± 0.5
Mg	5177	-1.66 ± 0.39	-3.6 ± 0.8
Na	5896	-4.07 ± 0.22	-7.3 ± 0.4
[O I]	6302	1.97 ± 0.42	3.5 ± 0.7
H α, [N II]	6565, 6585	7.24 ± 0.87	12.1 ± 1.5
[S II]	6718, 6732	3.39 ± 0.37	6.0 ± 0.7
Ca II	8544	-1.41 ± 0.17	-2.5 ± 0.3
Ca II	8665	-1.15 ± 0.14	-2.0 ± 0.2
Paδ	10053	-0.65 ± 0.10	-1.1 ± 0.2

Notes.

[a] The flux measurements are as observed in a single slitlet, i.e., not corrected for magnification due to gravitational lensing, underlying stellar absorption, dust extinction, or slit losses. Frye et al. (2024) first identified the lines listed and showed spectra of host-galaxy Images A and C (labeling them Arc 2a and 2c, respectively). They also gave the Hα line flux with corrections for underlying stellar absorption, dust extinction, and slit loss of the whole arc.

[b] Rest-frame equivalent widths (EWs) of emission and absorption lines.

[c] Negative fluxes and EWs indicate absorption lines, the latter opposite to the usual convention.

Table 2
Supernova Templates That Fit the Observed Spectra from the `NGSF` Analysis

Template	Type	Subtype	Phase	A_V	χ^2_ν
Image B					
SN 2013dy	Ia	Ia-norm	6.2	0.4	1.71
SN 2012cg	Ia	Ia-norm	9.6	0.0	2.18
SN 2000cx	Ia	Ia-pec	0.4	0.0	2.60
SN 2013dy	Ia	Ia-norm	0.0	0.0	2.70
SN 2012fr	Ia	Ia-norm	2.3	1.8	2.77
Image C					
SN 1994D	Ia	Ia-norm	28.6	0.1	0.69
SN 2013dy	Ia	Ia-norm	41.3	1.3	0.76
SN 2012cg	Ia	Ia-norm	38.6	0.8	0.77
SN 1991T	Ia	Ia-91T	40.0	0.6	0.78
SN 2011by	Ia	Ia-norm	30.3	0.3	0.79

Note. Columns show the template names, types, subtypes, phases (rest-frame days after peak brightness) for Image B or C as indicated, host extinction A_V, and reduced chi-square of the fit to the SN H0pe spectrum. Rows show the five best-match SN templates from the `NGSF` analysis.

Table 3
Supernova Templates That Fit the Observed Spectra from the `SNID` Analysis

Template	Type	Subtype	Phase	$r \times$ lap
Image B				
SN 2003ch	Ia	Ia-norm	1.8	9.15
SN 2003du	Ia	Ia-norm	−0.3	8.76
SN 2003du	Ia	Ia-norm	−1.3	8.47
SN 1996ai	Ia	Ia-norm	2.2	8.02
SN 2003du	Ia	Ia-norm	−2.2	7.95
Image C				
SN 1995al	Ia	Ia-norm	25.2	9.16
SN 1999aa	Ia	Ia-91T	25.2	7.57
SN 2000cx	Ia	Ia-pec	40.4	7.48
SN 2003cg	Ia	Ia-norm	42.9	7.42
SN 2005cf	Ia	Ia-norm	25.1	7.36

Note. Columns show the template names, types, subtypes, phases (rest-frame days after peak brightness) for Image B or C as indicated, and the $r \times$ lap values of the correlation with the SN H0pe spectrum. The $r \times$ lap value has been used in Blondin & Tonry (2007) to indicate the correlation, where r is the correlation height-to-noise ratio (Tonry & Davis 1979) and lap is the overlap in the logarithmic wavelength space between the SN spectrum and each of the template spectra used in the correlation. Rows show the five highest-correlated SN templates from the `SNID` analysis.

All of constraints on the phases were obtained while the authors were blind to those obtained from fitting the images' light curves (Pierel et al. 2024). Therefore the analysis presented herein is entirely independent of the light-curve phases. Only after completion of both analyses were the two sets of results unblinded by a third party and an inference for H_0 made (Pascale et al. 2024).

5.1. Hsiao07 Type Ia Supernova Spectral Template

We fit the spectra of the three SN images simultaneously with a shared set of parameters. The fit includes a total of 11 free parameters: the overall normalization α; the dust-extinction parameters $E(B - V)$ and R_V; the pair of flux ratios between Images A and B (f_A/f_B) and between Images A and C (f_A/f_C); the image phases $t_{\rm A}$, $t_{\rm B}$, and $t_{\rm C}$ at the time of observation; and a free background value for each of the three spectra. We use the `emcee` software package (Foreman-Mackey et al. 2013) to sample the model parameters and the implementation of the Hsiao07 templates in the `SNCosmo`

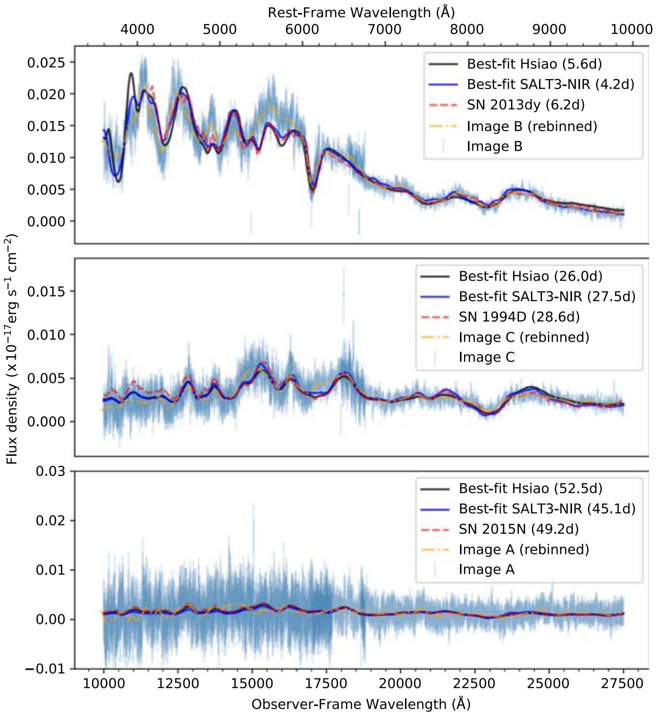

Figure 5. Best-fit templates and phases for the three images of SN H0pe as shown in the legends. Thin blue lines, merging into color bands, show 1σ error bars. Dashed–dotted orange lines show the observed spectra rebinned to 120 Å. Solid black lines show the best-fit Hsiao07 spectra. Solid blue lines show the best-fit SALT3-NIR model at each phase. Red dashed lines show the spectra of previously observed SNe Ia that most closely match the observed spectra of SN H0pe from our `NGSF` analysis.

package (Barbary et al. 2023). As a test, we also fit the Hsiao07 templates to each SN spectrum separately. Each of these fits had four model parameters: α, $E(B-V)$, R_V, and t_i, where t_i is the phase of that image. These results are also listed in Table B1 and are consistent with the shared-parameter results. Table B1 gives the derived phases, and the black curves in Figure 5 show the best fits. The posterior distributions of the fitted parameters are shown in Figure 6, and Figure 7 illustrates the fit uncertainties.

In the SN spectrum of Image B, as shown in Figures 5 and 7, the most notable deviation between the observed data and the best-fit model occurs in the rest-frame wavelength range of 5500–6000 Å. This discrepancy could be attributed to the diversity in the continuum level of SNe Ia near the Si II λ5972 feature or potentially to incomplete modeling of magnesium and sodium features during host-galaxy subtraction. The latter might suggest a color gradient within the host galaxy of SN H0pe. Given that our current extraction technique does not account for the color gradient of extended sources, we anticipate that future spectroscopic observations of the host galaxy, conducted in the absence of the SN, will provide insights into this observed discrepancy.

5.2. SALT3-NIR Model

For the SALT3-NIR (Pierel et al. 2022) analysis, the input parameters for this model are the overall normalization x_0, a light-curve shape parameter ("stretch") x_1, a color parameter c, and the phase and background parameters as for the analysis using the Hsiao07 template. Because the SALT3-NIR model is limited to phases $\leqslant 50$ days, for larger phases, we assigned likelihoods equal to the 50 day value. As for the Hsiao07 templates, we tested independent fits to each spectrum in addition to the primary simultaneous fit to all three spectra. Figure 5 shows the best fits of the SALT3-NIR model to the spectra, and Table B1 lists the best-fit image phases. Appendix C presents the full results of the SALT3-NIR model fitting including parameter distributions and uncertainties.

The SALT3-NIR results are statistically consistent with those from the Hsiao07-template analysis. However, the phase of Image A from the SALT3-NIR fitting approaches the 50 day upper validity limit of the model. For the joint fitting, this proximity to the limit of the model may affect the SALT3-NIR model's constraints on the other image phases, potentially leading to biased estimates of the time delays and magnifications. Therefore, we do not rely on the joint SALT3-NIR fitting for our primary constraints on the phases or relative time delays of the images.

5.3. `SNID`

As a third measurement, we derive constraints *independent* of the SN color, i.e., using only the spectral features. For this, we employed `SNID` (Blondin & Tonry 2007), which removes the continuum from the SN spectrum before cross-correlating the SN spectrum with template spectra. We used both the built-in `SNID` template library ("template 2.0") and a library that we constructed from the SALT3-NIR SN Ia template, which includes 1750 spectra across 70 SN phases, each spanning 25 different combinations of the stretch (x_1) and color (c) parameters. Figure 8 plots the continuum-removed spectra of Images B and C superimposed on the 100 best-fitting SN spectra.

For the Image B spectrum, the matching templates all have early phases (Table B1) but are consistent with the Hsiao07 and SALT3-NIR results within the uncertainties (Table B1). Using the simulated templates generated from the SALT3-NIR model gives phases and uncertainties similar to those from the templates 2.0 package but with a preference for a slightly later phase for Image B (Table B1).

The `SNID` analysis provides decisive evidence that SN H0pe is Type Ia. All SN phases from the `SNID` analysis are consistent with the values from the SALT3-NIR and Hsiao07 analyses, but the uncertainties are larger than those from Hsiao07 or SALT3-NIR.

6. Uncertainties of the Measurements of Time Delays and Magnifications

Image A might be at a phase outside the SALT3-NIR model's validity range, and the image is too faint for `SNID` to reliably infer its phase. This leaves the Hsiao07 templates as the principal basis for our analysis. To assess the templates' ability to determine SN phases, our analysis began with joint fitting of a set of well-observed, nearby SNe Ia with the Hsiao07 templates, as described in Section 6.1. Section 6.2 presents the subsequent modeling of the effects of millilensing and microlensing to assess those processes' impacts on the time-delay and magnification measurements. Final constraints on the SN phases, magnifications, and relative time delays are presented in Section 7.

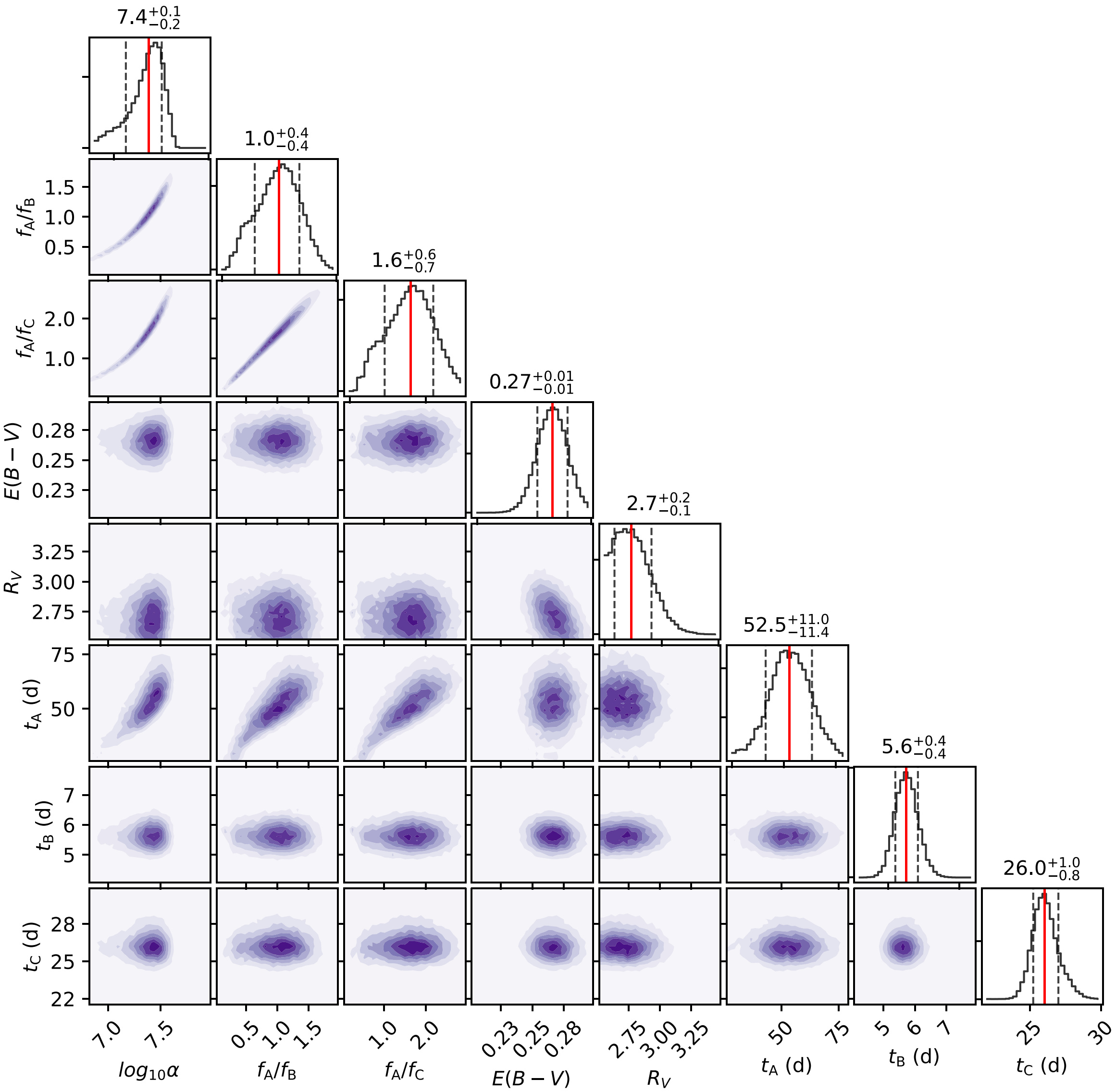

Figure 6. Parameter distributions from the Hsiao07-template fits. α, R_V, and $E(B-V)$ are model parameters (Section 5.1), f_A/f_B and f_A/f_C are template-flux ratios between Images A and B and between Images A and C, respectively, and t_A, t_B, and t_C are rest-frame phases of Images A, B, and C, respectively. The solid vertical line on each histogram marks the median of the parameter, while the dashed vertical lines denote the 68% confidence interval of each distribution.

6.1. Simulation of the Hsiao07 Modeling

To assess the ability of the Hsiao07 templates to recover the phase of the SN images, we applied the same analysis to the spectra of a set of well-observed, nearby SNe Ia listed in `SNID`'s built-in library. The SNe were chosen to have at least one spectrum in each of the following ranges of phase relative to maximum: (−10, 10), (10, 30), and (30, 60) days. These ranges correspond to the values inferred for SN H0pe Images B, C, and A, respectively, using the Hsiao07 templates, which include spectra through 80 days. This gave 228 sets of spectra for the simulation with each set consisting of three SN spectra in the three phase bins. To each spectrum, we added the residuals of the NIRSpec spectra from the smoothed spectra (as shown by the dashed–dotted lines in Figure 5), drawing randomly from the residual distribution across all wavelengths. This step assumes the residuals are random rather than correlated with wavelength. Additionally, we rescaled the spectra to match the signal-to-noise ratio of the NIRSpec observations.

Figure 9 compares the actual and inferred phases. The residuals and the confidence intervals, shown by shaded areas, are plotted in the right panels of Figure 9. As shown in Figure 9, the inferred phase is generally in agreement with the true value, and the agreement is especially good at phases <30 days. Beyond 30 days, the uncertainty associated with the inferred phase is significantly greater, primarily because of Image A's low signal-to-noise ratio and the slow evolution of SN spectral features at these phases.

6.2. Millilensing and Microlensing

Lens-model predictions of the image magnification ratios and relative time delays include only structure on the scale of galaxy members and the cluster itself. Therefore, the effects of millilensing by subhalos and microlensing by stars and compact objects have to be included in the uncertainties on the inferred phases and time delays. Millilenses affect only the magnifications of the SN images because the SN photosphere ($\sim 10^{14}$–10^{15} cm in radius) is much smaller than the scale of a

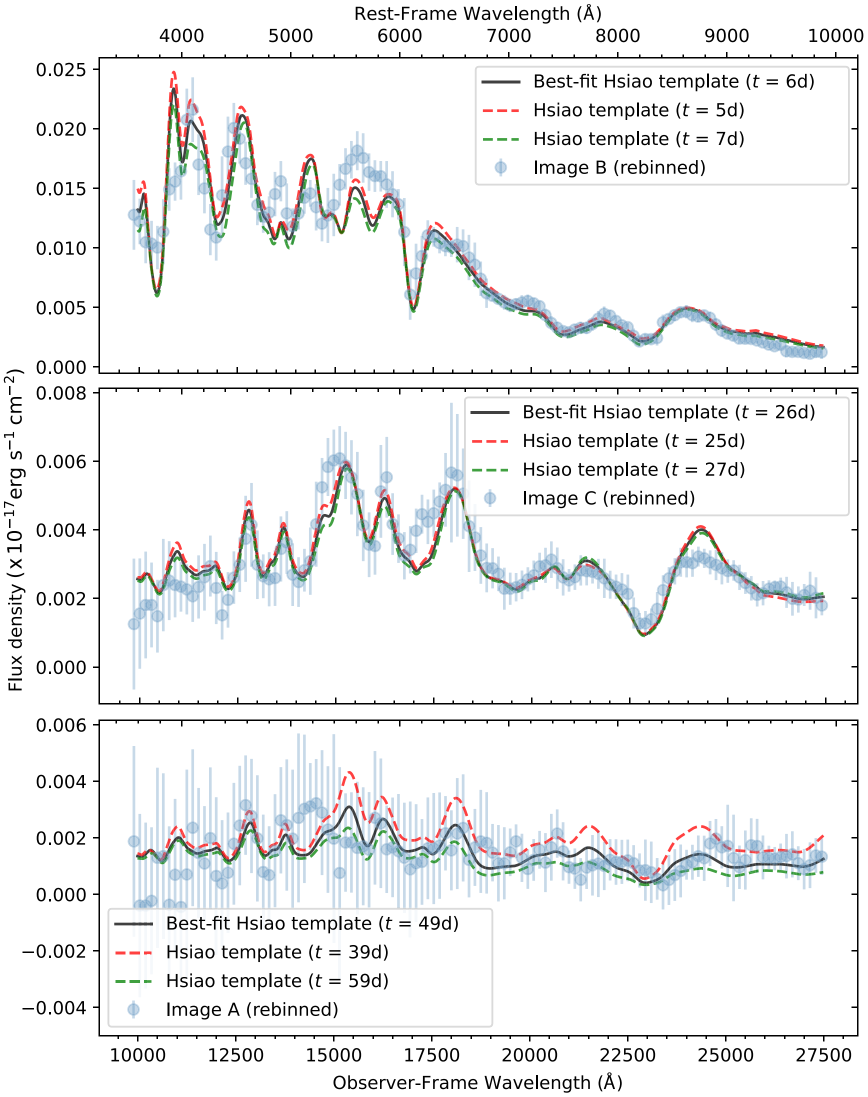

Figure 7. Best-fit Hsiao07 templates from Figure 5 are depicted again here, including the models for SN phases that deviate by ±1σ (rounded to the nearest integers) from the best-fit phases. Data points and error bars show the observed (rebinned to 120 Å) SN H0pe spectra.

millilens caustic. Microlenses, such as stars and stellar remnants, on the other hand, have Einstein radii comparable to the size of the SN photosphere. As the expanding SN photosphere crosses a microlens caustic, different portions of the photosphere can be magnified differently, leading to wavelength-dependent changes in the SN spectrum (Foxley-Marrable et al. 2018; Goldstein et al. 2018; Huber et al. 2019). Consequently, microlensing can affect not only the magnification of the SN images but also the time-delay estimates.

To compute the uncertainties due to microlensing and millilensing, we utilized 4000 simulations of SN Ia spectra.[22] In brief, for each of the four theoretical models of microlensing caustics from Suyu et al. (2020) and Huber et al. (2021), a set of SNe Ia were placed at 1000 random positions in the source plane. The simulated spectrum at each position compared to the input spectrum without microlensing was used to determine the wavelength-dependent magnification due to microlensing. The millilens magnification distributions were calculated for a range of dark matter subhalo mass functions and substructure fractions anticipated from theory as well as observations (Gilman et al. 2020). A magnification drawn from one of the millilensing distributions was applied to each simulated SN sight line. As in Section 6.1, we added noise to the simulated spectra to match the signal-to-noise ratios of the three SN H0pe spectra. Then we simultaneously fit the set of three simulated spectra corresponding to the three SN H0pe images. The differences between the inferred and input SN phases and magnifications yielded an estimate of the systematic uncertainties arising from millilensing and microlensing. Table 4 gives the results.

7. Constraints on Time Delays and Magnifications

To obtain accurate inferences about the phases of the spectra of the three images of the SN, we combine the parameter values in the MCMC chain together with the results of our simulations. In our simulations, we measure the residuals of the recovered phases from the input phases of SN. Here we use the residuals we measure to correct the parameter values in the MCMC chain for bias and account for systematic uncertainty. For our joint fitting using the Hsiao07 templates, for each *i*th

---

[22] The simulations are described in detail in the companion paper presenting time-delay inferences from the photometry of the SN: Pierel et al. (2024).

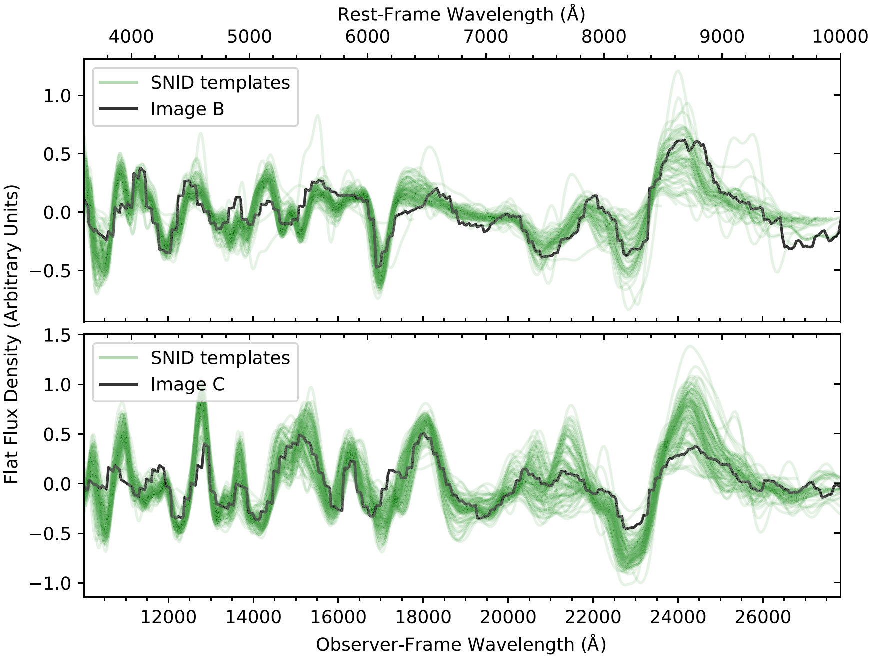

Figure 8. Flattened flux density of SN Images B and C used for the `SNID` analysis (black). Green curves show the 100 best-fitting `SNID` templates.

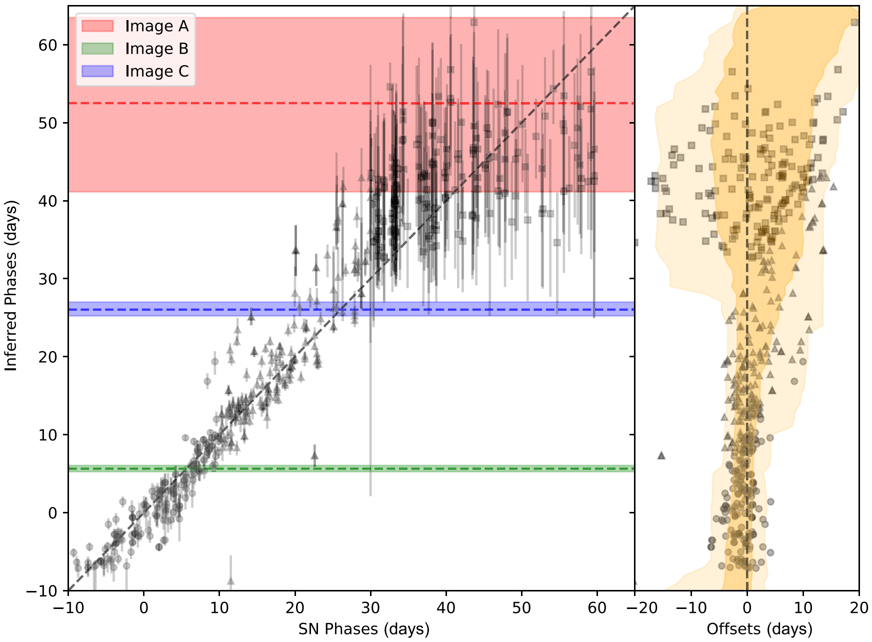

Figure 9. Left: inferred phases from Hsiao07 fitting vs. actual phases of a set of nearby SNe Ia. Error bars correspond to the 68% confidence intervals of the inferred phases. Horizontal dashed lines and shaded regions mark the inferred phases and their 68% confidence intervals for the three images of SN H0pe. The diagonal dashed line shows equality. Right: deviation of the best-fit inferred phase from the actual phase. Shaded regions mark the 68% (darker) and 95% (lighter) confidence intervals of the residuals measured within a 10 day rolling window. Data points marked by squares, circles, and triangles correspond to spectra with signal-to-noise ratios matching those of Images A, B, and C, respectively (as described in Section 6.1). Simulations including input SNe beyond 60 days could, in principle, increase the uncertainty for Image A, and constraints will benefit from future simultaneous measurement from spectra and imaging.

Table 4
Microlensing and Millilensing Uncertainties

σ_m (±AB magnitude)	Image A	Image B	Image C
Microlensing	0.04	0.12	0.04
Millilensing	0.04	0.04	0.04

Note. Median standard deviation of magnitude changes σ_m across the rest-frame wavelength range 3600 to 10000 Å in the simulated SN Ia sample.

step in the MCMC chain from our joint fitting, we obtained a set of eight model parameters, denoted as $\boldsymbol{X}^i = [\alpha^i_{\rm A}, \alpha^i_{\rm B}, \alpha^i_{\rm C}, E(B-V)^i, R^i_V, t^i_{\rm A}, t^i_{\rm B}, t^i_{\rm C}]$. The alphas are related to the ones described in Section 5.1 by $\alpha^i_{\rm A} = \alpha^i$, $\alpha^i_{\rm B} = \alpha^i/(f_{\rm A}/f_{\rm B})^i$, and $\alpha^i_{\rm C} = \alpha^i/(f_{\rm A}/f_{\rm C})^i$. We proceeded by randomly selecting an SN among the SNe Ia with an inferred phase within a ±10 day window and calculating the median offsets of this SN's inferred phase from its actual value. Next,

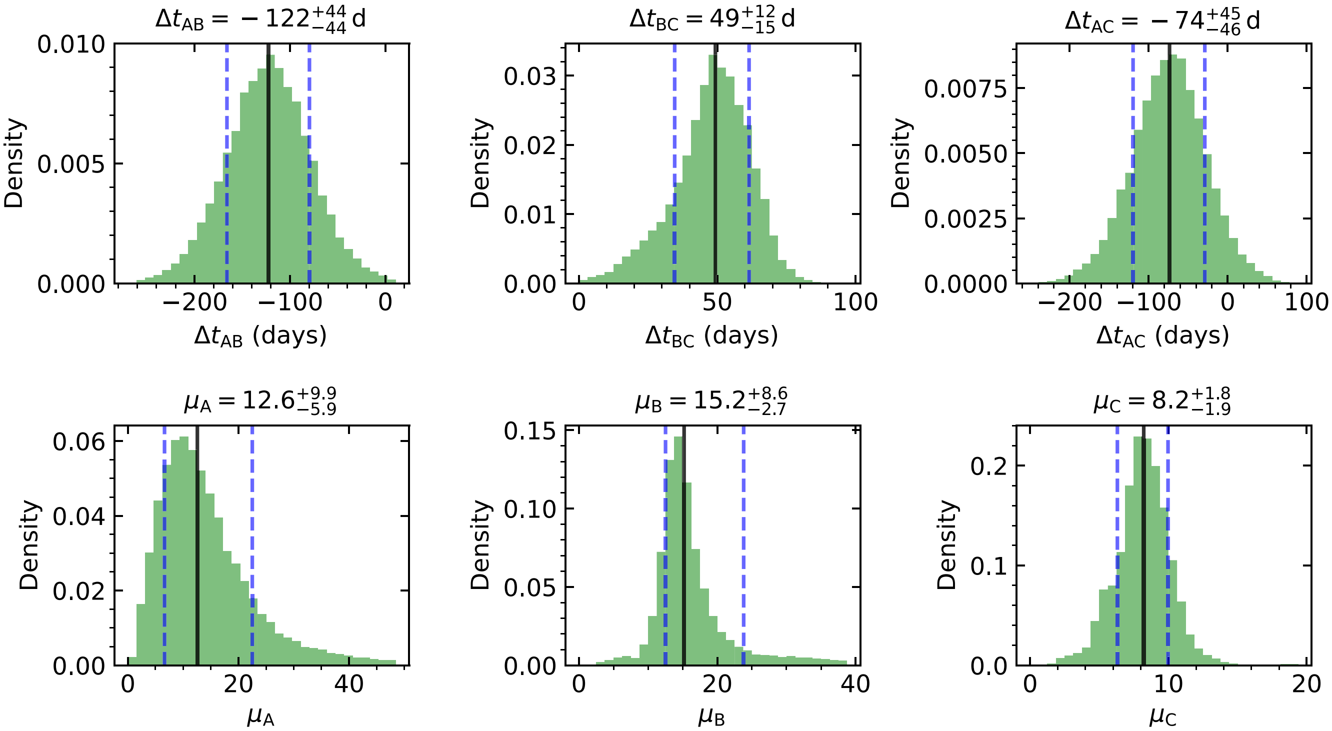

Figure 10. Posterior probability densities of the relative time delays and the macrolens magnifications between SN H0pe's images. Histograms show the values derived from the Hsiao07 templates. The distributions integrate the uncertainty from the MCMC fitting with systematic uncertainties, estimated from the model fitting of nearby SN Ia spectra and from the simulated SN Ia spectra. The uncertainties take into account the impacts of microlensing and millilensing effects.

Table 5
Y-band Apparent AB Magnitudes of the Supernova Images

$i =$	A	B	C
	Magnitudes from the Hsiao07 fits		
	$25.41^{+0.45}_{-0.32}$	$24.60^{+0.05}_{-0.05}$	$24.84^{+0.06}_{-0.06}$
	Predicted magnitudes for $t_i = 0$		
	$24.39^{+0.69}_{-0.63}$	$24.18^{+0.22}_{-0.48}$	$24.85^{+0.29}_{-0.21}$

Note. The rest-frame *Y*-band photometry was synthesized using the Dark Energy Camera's *Y* filter (Abbott et al. 2018) set at airmass 1.3 based on the Hsiao07-template fits. Phases t_i are rest-frame days after the peak brightness in the rest-frame *B* band.

we chose a set of three SN spectra from our simulated millilensing and microlensing samples and determined the median offsets between the input and inferred parameter values. These offsets, derived from the simulations, were then applied to the parameters in the MCMC chain. This process resulted in a modified set of eight parameters $\boldsymbol{Y}^i$, where $Y_1^i = \alpha_{\rm A}^i + \delta\alpha_{\rm A}^j + \delta\alpha_{\rm A}^k$, $Y_2^i = \alpha_{\rm B}^i + \delta\alpha_{\rm B}^j + \delta\alpha_{\rm B}^k$, $Y_3^i = \alpha_{\rm C}^i + \delta\alpha_{\rm C}^j + \delta\alpha_{\rm C}^k$, $Y_4^i = E(B-V)^i + \delta E(B-V)^k$, $Y_5^i = R_V^i + \delta R_V^k$, $Y_6^i = t_{\rm A}^i + \delta t_{\rm A}^j + \delta t_{\rm A}^k$, $Y_7^i = t_{\rm B}^i + \delta t_{\rm B}^j + \delta t_{\rm B}^k$ and $Y_8^i = t_{\rm C}^i + \delta t_{\rm C}^j + \delta t_{\rm C}^k$. Here the *j* and *k* indices are for the set of randomly selected SN spectra from the low-redshift SN Ia simulation and from the millilensing and microlensing simulation, respectively. For the simulation of the low-redshift SNe Ia, we assume that the extinction parameters R_V and$E(B-V)$ were fit accurately for each SN.

To constrain the absolute magnifications of the three images of the SN, we used the MCMC sample from our joint fitting. For each set of modified model parameters $\boldsymbol{Y}^i$ in the MCMC chain at the *i*th step, we generated a set of three synthetic SN spectra using the `SNCosmo` package (Barbary et al. 2023).

The expected rest-frame *B*-band magnitudes of SNe Ia were obtained from the complete sample of Scolnic et al. (2018). To estimate $\hat{m}_B$ at $z = 1.782$ independent of the cosmological distance and H_0, we used a polynomial fit to interpolate $\hat{m}_B$ as a function of the logarithmic redshift, which yields $\hat{m}_B = 26.32 \pm 0.03$ at $z = 1.782$. As a cross-check performed after unblinding, a concordance cosmology described by the Lambda cold dark matter model (ΛCDM) with $\Omega_{\rm m} = 0.3$, $\Omega_\Lambda = 0.7$, and a Hubble constant $H_0 = 70$ km s^{-1} Mpc^{-1} yields $\hat{m}_B = 26.30$ at the redshift.

The magnitude in a specific band for a given amplitude of the model is dependent upon host-galaxy extinction. In our analysis using the Hsiao07 templates, we assumed that SN H0pe is a standard candle in the rest-frame *Y* band, where previous studies (e.g., Avelino et al. 2019) show that the SN brightness is not substantially correlated with the spectral stretch and color and is homogeneous without these corrections. We then determined the expected *Y*-band magnitude for an unmagnified SN Ia. For an SN Ia spectrum produced by the Hsiao07 templates with the best-fit dust-extinction parameters, we varied the normalization factor of the spectrum to match its *Y*-band magnitude to that of an SN Ia without extinction and with a rest-frame *B*-band magnitude ($\hat{m}_B$) equal to the expected value. This yielded an unlensed *Y*-band magnitude of 27.15 ± 0.03. Subsequently, we synthesized a *Y*-band measurement of the SN for each set of parameters $\boldsymbol{Y}^i$ in the MCMC chain and calculated the predicted *Y*-band magnitude at the SN phase $t = 0$ for each image based on the Hsiao07 templates. We then determined the magnification by comparing the resultant *Y*-band magnitude to the expected

Table 6
Correlation Matrices of the Model Parameters

	$\Delta t_{\rm AB}$	$\Delta t_{\rm BC}$	$\Delta t_{\rm AC}$	$\mu_{\rm A}/\mu_{\rm B}$	$\mu_{\rm B}/\mu_{\rm C}$	$\mu_{\rm A}/\mu_{\rm C}$	$\mu_{\rm A}$	$\mu_{\rm B}$	$\mu_{\rm C}$
Hsiao07									
$\Delta t_{\rm AB}$	1.000								
$\Delta t_{\rm BC}$	−0.002	1.000							
$\Delta t_{\rm BC}$	0.947	0.320	1.000						
$\mu_{\rm A}/\mu_{\rm B}$	−0.572	0.086	−0.514	1.000					
$\mu_{\rm B}/\mu_{\rm C}$	−0.268	−0.457	−0.402	−0.178	1.000				
$\mu_{\rm A}/\mu_{\rm C}$	−0.633	−0.304	−0.698	0.420	0.678	1.000			
$\mu_{\rm A}$	−0.721	−0.131	−0.725	0.480	0.525	0.872	1.000		
$\mu_{\rm B}$	−0.322	−0.223	−0.394	−0.202	0.851	0.535	0.622	1.000	
$\mu_{\rm C}$	−0.020	0.651	0.191	0.009	−0.800	−0.321	0.021	0.022	1.000
SALT3-NIR									
$\Delta t_{\rm AB}$	1.000								
$\Delta t_{\rm BC}$	−0.082	1.000							
$\Delta t_{\rm BC}$	0.932	0.284	1.000						
$\mu_{\rm A}/\mu_{\rm B}$	−0.467	0.065	−0.426	1.000					
$\mu_{\rm B}/\mu_{\rm C}$	−0.055	−0.243	−0.141	−0.409	1.000				
$\mu_{\rm A}/\mu_{\rm C}$	−0.516	−0.244	−0.585	0.516	0.317	1.000			
$\mu_{\rm A}$	−0.639	−0.030	−0.626	0.683	0.101	0.797	1.000		
$\mu_{\rm B}$	−0.053	−0.120	−0.095	−0.477	0.898	0.127	0.112	1.000	
$\mu_{\rm C}$	0.018	0.588	0.231	0.014	−0.357	−0.458	0.001	−0.070	1.000

Note. Each *i*th row and *j*th column is the correlation between the *i*th and *j*th parameters. The upper section of the table is for the Hsiao07 models (Section 5.1), and the lower section is for the SALT3-NIR models (Section 5.2). Parameters are the relative time delays $\Delta t_{\rm AB}$, $\Delta t_{\rm BC}$, and $\Delta t_{\rm AC}$, the magnification ratios $\mu_{\rm A}/\mu_{\rm B}$, $\mu_{\rm B}/\mu_{\rm C}$, and $\mu_{\rm A}/\mu_{\rm C}$, and the magnifications $\mu_{\rm A}$, $\mu_{\rm B}$, and $\mu_{\rm C}$.

Table 7
Final Constraints on the Phases and Magnifications of the SN Images

$i =$	A	B	C	Blinded
Hsiao07-template fits				
t_i	$50.6^{+16.1}_{-15.3}$ days	$6.5^{+2.4}_{-1.8}$ days	$24.3^{+3.9}_{-3.9}$ days	Y
t_i	$54.5^{+18.7}_{-17.0}$ days	$6.2^{+2.5}_{-1.7}$ days	$24.5^{+3.6}_{-3.4}$ days	N
μ_i	$12.6^{+9.9}_{-5.9}$	$15.2^{+8.6}_{-2.7}$	$8.2^{+1.8}_{-1.9}$	Y
μ_i	$14.5^{+13.3}_{-7.1}$	$15.3^{+8.2}_{-2.7}$	$8.4^{+1.7}_{-1.7}$	N
SALT3-NIR fits				
t_i	$42.8^{+11.4}_{-9.7}$ days	$5.6^{+2.3}_{-2.1}$ days	$26.7^{+2.5}_{-4.2}$ days	Y
μ_i	$9.3^{+5.2}_{-3.7}$	$16.2^{+11.3}_{-3.2}$	$10.3^{+1.7}_{-2.0}$	Y
μ_i	$9.0^{+4.8}_{-3.6}$	$15.6^{+11.1}_{-3.0}$	$9.8^{+1.6}_{-2.0}$	Y

Note. Phases t_i are rest-frame days after the peak brightness. Magnifications μ_i are the macromagnifications from the cluster and are based on SN Ia absolute magnitudes as described in Section 7 for the Hsiao07 templates and Appendix C.3 for the SALT3-NIR fits. For the Hsiao07-template fits, the second row of t_i and μ_i are based on a postunblinding test where we expand the third phase bin for selecting the nearby SN Ia spectra from (30, 60) days to (30, 80) days (as described in Section 8). For the SALT3-NIR fits, the first row of μ_i is based on *B*-band absolute magnitudes, and the second row is based on *Y* band.

value. Table 5 list the resultant *Y*-band magnitudes derived from the MCMC chain and the predicted magnitudes at $t = 0$.

Finally, we reconstructed the posterior distribution of the time delays and the macrolens magnifications (i.e., the magnifications from the cluster lens) as illustrated in Figure 10. Table 6 lists the correlation matrices of the relative time delays, magnification ratios, and magnifications from our analysis using the Hsiao07 template. Our final constraints on the SN phases, magnifications, and relative time delays are listed in Tables 7 and 8.

Table 8
Final Constraints on the Relative time Delays

$i =$	AB	BC	AC	Blinded
Hsiao07-template fits				
Δt_i	$-122.3^{+43.7}_{-43.8}$ days	$49.3^{+12.2}_{-14.7}$ days	$-73.6^{+44.7}_{-46.1}$ days	Y
Δt_i	$-133.8^{+47.2}_{-51.1}$ days	$50.3^{+12.0}_{-12.7}$ days	$-82.8^{+50.2}_{-54.6}$ days	N
SALT3-NIR fits				
Δt_i	$-103.6^{+27.9}_{-32.2}$ days	$57.7^{+10.2}_{-12.3}$ days	$-46.8^{+29.5}_{-33.7}$ days	Y

Note. Relative time delays Δt_i are days in the observer frame. For the Hsiao07-template fits, the second row of Δt_i is based on a postunblinding test where we expand the third phase bin for selecting the nearby SN Ia spectra from (30, 60) days to (30, 80) days (as described in Section 8).

8. Postunblinding Tests

As described in Section 6.1, we chose three bins in SN phase to select the spectra of nearby SNe Ia. These bins were determined a priori based on the result of the joint MCMC fitting, before we conducted the simulation. Given the low signal-to-noise ratio of Image A's spectrum, there is a lack of sensitivity to phases for SN Ia spectra with inferred phases beyond ∼40 days. To assess the impact of the upper limit of the third phase bin (assigned for Image A) on the inferred time delays and magnifications, we expanded the range of third phase bin from (30, 60) days to (30, 80) days. We then performed the same simulation as described in Section 6.1 with the extended phase bin, while keeping the results of the other simulations unchanged to determine the final constraints. Tables 7 and 8 list the resulting constraints on the phases, the magnifications, and the relative time delays of SN H0pe's images. Figure 11 shows the distributions of these parameters, overplotted on the preunblinding distributions. This test was

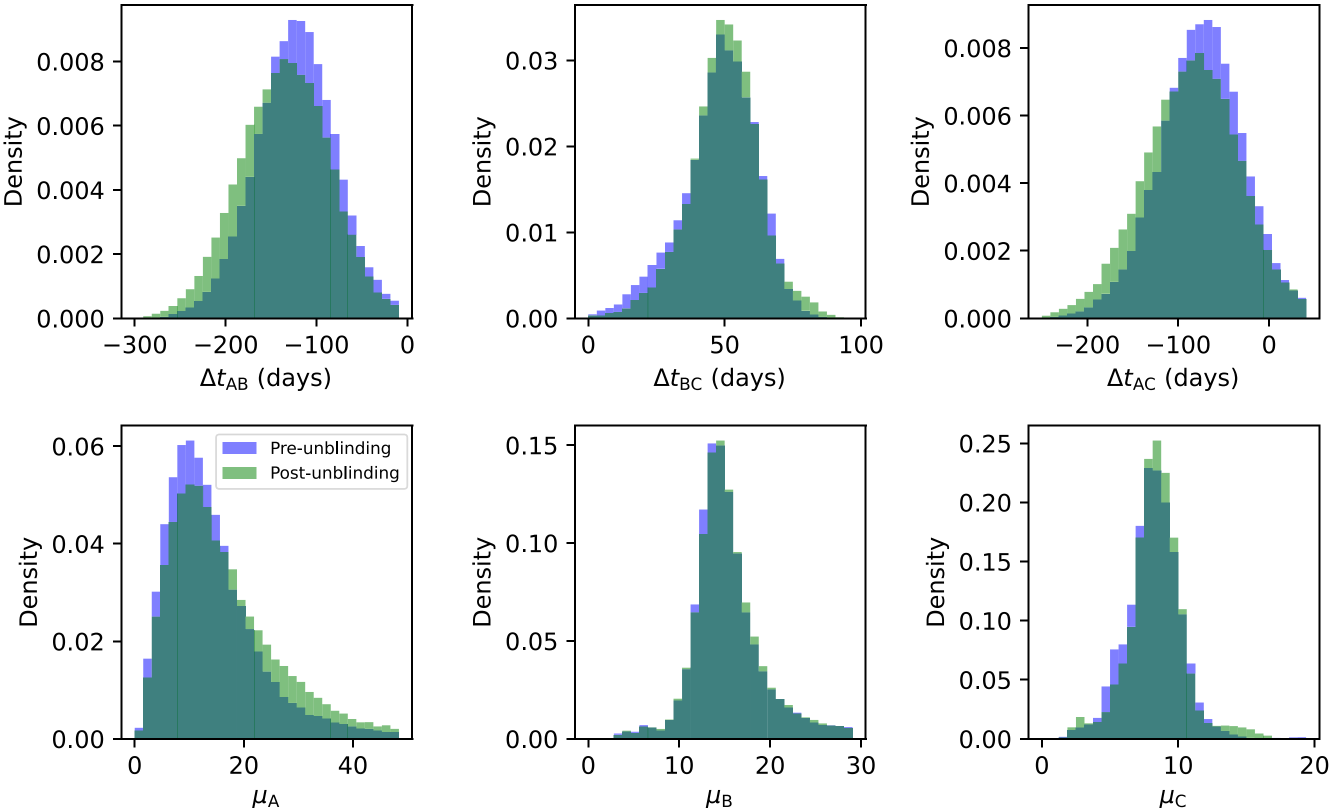

Figure 11. Posterior probability densities of the relative time delays and the macrolens' magnifications between SN H0pe's images. For the preunblinding result, we simulated the joint Hsiao07-template fitting by selecting a set of three spectra from three SN phase bins: (−10, 10), (10, 30), and (30, 60) days (as described in Section 6.1). For the postunblinding test, we expand the third phase bin to (30, 80) days.

conducted after the unblinding of the result from the H_0-inference team (Pascale et al. 2024).

As shown in Figure 11, the distributions of relative time delays and magnifications remain largely unaffected by the adjustment of the upper limit, for which the deviations of the corresponding distributions are much smaller compared to the uncertainties of these measurements. Given the slightly longer time delays compared to the original result, the inferred H_0 will be ∼3% smaller than that based on the preunblinding constraints. However, the difference is only $\sim 0.1\sigma$, which is not statistically substantial. For the H_0 inference by Pascale et al. (2024) based on the time-delay measurements from both the spectroscopic and photometric analyses, the impact of the upper limit of the phase bin for our simulation is minimal (<1%).

We note that the analysis we performed before unblinding does not include an uncertainty associated with the phases of well-observed, nearby SNe Ia, as the uncertainty of determining the phase at peak brightness based on a well-sampled light curve is less than 1 day (Riess et al. 1997), which is much smaller than that from fitting the Hsiao07 templates to individual spectra of SN H0pe (approximately 5 days, as demonstrated in Section 6.1). To assess the impact of the time-delay measurement arising from the phases of the nearby SNe Ia, we include a normally distributed offset with a standard deviation of 1 day to each nearby SN used in our simulation and repeated the analysis that we conducted prior to the unblinding. Compared to the results from our blind analysis, the addition of this uncertainty does not affect the inferred phases and magnifications of the SN H0pe images, and the size of the 68% confidence intervals increases by only $\lesssim 7\%$.

In addition, there are two outliers in the left panel of Figure 9, which correspond to SN 2001N at a phase of 11.5 days and SN 2002do at 22.6 days. Repeating the analysis excluding these two SNe changes the best-fit SN phases by only $\lesssim 0.01\sigma$, and the impact on the 68% confidence intervals is negligible.

9. Conclusions

All of our analyses of the spectra of SN H0pe classify SN H0pe as an SN Ia and favor a "normal" (Blondin & Tonry 2007) subtype. The velocity of the Si II $\lambda 6355$ absorption line is consistent with a normal-velocity SN Ia. The SN phases and relative time delays are constrained with 1σ uncertainties of 2–4 days for Images B and C and 2 weeks for the latest-arriving Image A.

Our analyses using the Hsiao07 templates, the SALT3-NIR model, and the `SNID` software package yield consistent results for the phases of the SN images. The relative time delays between the three SN H0pe images and their magnifications, as derived from our analyses based on the Hsiao07 templates and the SALT3-NIR model, are statistically in agreement. However, the inferred phase of Image A is near or above the upper boundary of the SALT3-NIR model's validity range. During the joint fitting, this affected the constraints of the SALT3-NIR model, potentially biasing the estimates of the time delays and magnifications. The `SNID` model approach, which was unable to utilize the information from the faintest Image A, yielded larger uncertainties than the Hsiao07 analysis but only uses the spectral features, since the SN continuum is subtracted.

In addition to time delays and magnifications, the fits using the Hsiao07 templates constrain the host extinction to $E(B-V)=0.27\pm0.02$ and $R_V=2.73\pm0.17$. The $E(B-V)$ is consistent with the values listed in Table 4 of Frye et al. (2024). This indicates that the SN exploded in a relatively dusty environment with an extinction $A_V\gtrsim0.7$.

SN H0pe will be valuable not only for measuring the Hubble–Lemaître constant but also, because this is the second-highest currently known redshift SN Ia, for testing whether SNe at large lookback times had the same properties as SNe today. Based on spectra at multiple rest-frame epochs, SN H0pe matches the most common type of SNe Ia in the nearby Universe. Our analysis of the SN images' phases, based solely on the NIRSpec spectra, suggests a relative uncertainty of $\gtrsim$20% in the time delay between the two brightest images (B and C). This would limit the precision of constraints on the Hubble constant from the measured spectroscopic time delay to $\gtrsim$20%, given more precise lens model predictions. Beyond the blind analysis detailed in this paper and the associated photometric-analysis paper (Pierel et al. 2024), a comprehensive joint analysis—utilizing both the spectroscopic time delay and the photometric measurements (Pascale et al. 2024)—will yield a combined measurement of the Hubble constant with improved precision. Finally, we expect future data challenges using synthetic spectra, light curves, and galaxy-cluster mass models of multiply imaged SNe, similar to those conducted for galaxy-lensed active galactic nuclei (e.g., Dobler et al. 2015; Ding et al. 2021), will further improve our understanding of the systematic uncertainties in measuring the Hubble constant using cluster-lensed SNe.

Acknowledgments

This work is based on observations made with the NASA/ESA/CSA JWST. The data were obtained from the Mikulski Archive for Space Telescopes (MAST) at the Space Telescope Science Institute, which is operated by the Association of Universities for Research in Astronomy, Inc., under NASA contract NAS 5-03127 for JWST. These observations are associated with program JWST DDT 4446. R.A.W. and S.H.C. acknowledge support from NASA JWST Interdisciplinary Scientist grants NAG5-12460, NNX14AN10G, and 80NSSC18K0200 from GSFC. A.Z. acknowledges support by grant No. 2020750 from the United States-Israel Binational Science Foundation (BSF) and grant No. 2109066 from the United States National Science Foundation (NSF); by the Ministry of Science & Technology, Israel; and by the Israel Science Foundation grant No. 864/23. S.H. thanks the Max Planck Society for support through the Max Planck Research Group for S. H. Suyu and the European Research Council (ERC) under the European Union's Horizon 2020 research and innovation program (grant agreement No. 771776) for funding. C.L. acknowledges support from the National Science Foundation Graduate Research Fellowship under grant No. DGE-2233066. P.L.K. acknowledges funding from NSF grants AST-1908823 and AST-2308051. The authors thank the anonymous referee for the valuable comments and suggestions.

Data used in this paper can be retrieved at MAST: doi:10.17909/rqdx-3976.

Facility: JWST (NIRSpec spectroscopy and NIRCam imaging).

Software: jwst 1.10.2 (https://jwst-pipeline.readthedocs.io/en/latest/jwst/introduction.html), MOS Optimal Spectral Extraction (https://spacetelescope.github.io/jdat_notebooks/notebooks/optimal_extraction/Spectral_Extraction-static.html), sncosmo (https://sncosmo.readthedocs.io/en/stable/), emcee (https://emcee.readthedocs.io/en/stable/), NGSF (https://github.com/oyaron/NGSF), and SNID (https://people.lam.fr/blondin.stephane/software/snid/).

Appendix A
Background Subtraction, 2D Spectrum Modeling, and Source Extraction

Because the MSA slitlets used to observe SN H0pe are occupied by extended sources such as the SN's host galaxy, the default JWST pixel-to-pixel background subtraction based on in-scene and off-scene nods was skipped. In addition, the lack of "blank sky" shutters in this NIRSpec observation makes it hard to obtain a well-defined master background to feed to the JWST pipeline for subtraction. Instead, we developed a custom code to evaluate a 2D master background using the local minimum flux in 2D spectra for a given wavelength. In detail, for each pixel in a 2D spectrum without a background subtraction, we calculated the minimum flux from the pixels with MSA shutters in the same position along the slit direction. Because the minimum flux could be biased by bad pixels (e.g., cosmic-ray masks), we smoothed the resulting 2D minimum-

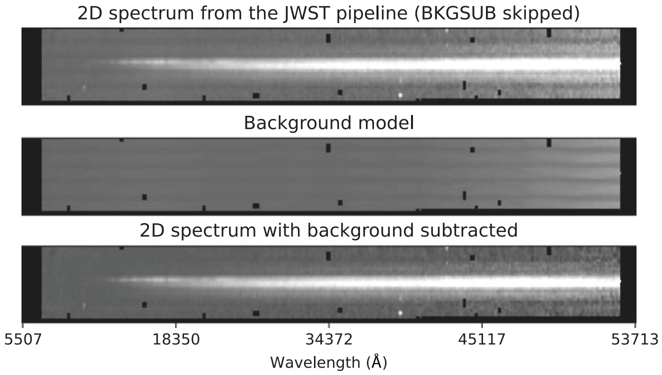

Figure A1. An example of the background subtraction. The top panel shows the 2D spectrum from the JWST pipeline with the background-subtraction step (BKGSUB) skipped. The middle panel shows the background model from the local-minimum-flux method. The bottom panel shows the residuals after subtracting the background model from the original spectrum.

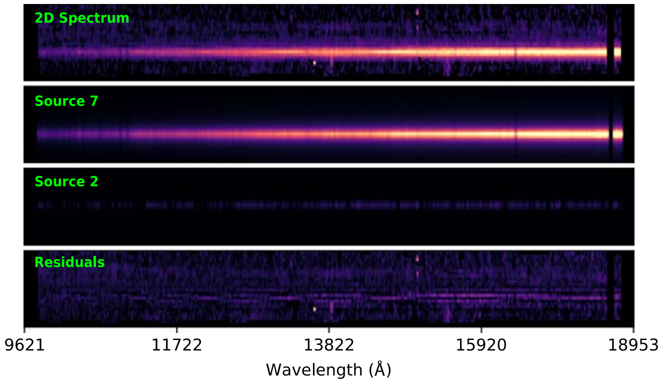

Figure A2. G140M spectrum from Slit A. The top panel shows the 2D spectrum from the JWST pipeline. The middle two panels show the best-fit models of the host galaxy (Source 7) and the SN (Source 2). The bottom panel shows the residuals after subtracting the galaxy and the SN model from the original spectrum.

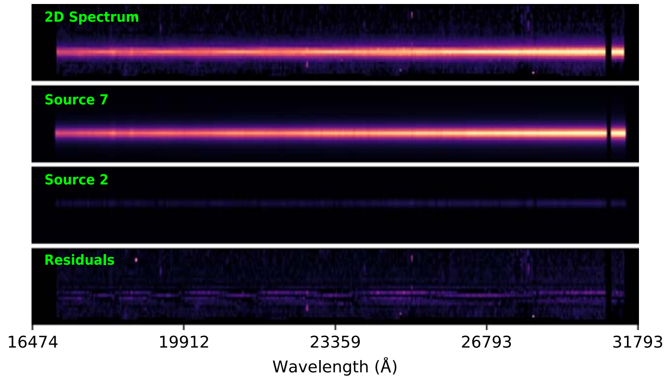

Figure A3. G235M spectrum from Slit A. The top panel is the 2D spectrum from the JWST pipeline. The middle two panels show the best-fit models of the host galaxy (Source 7) and the SN (Source 2). The bottom panel shows the residuals after subtracting the galaxy and the SN models from the original spectrum.

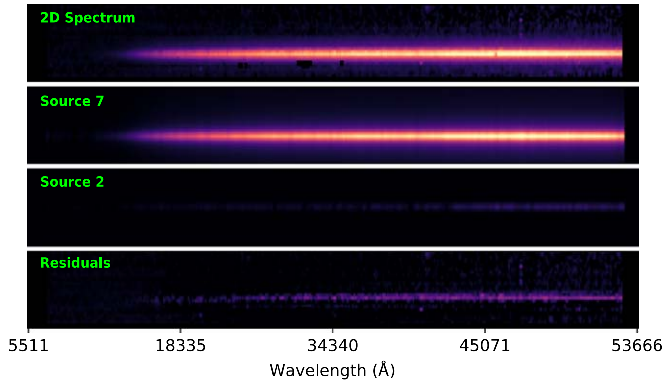

Figure A4. PRISM spectrum from Slit A. The top panel shows the 2D spectrum from the JWST pipeline. The middle two panels show the best-fit models of the host galaxy (Source 7) and the SN (Source 2). The bottom panel shows the residuals after subtracting the galaxy and the SN models from the original spectrum.

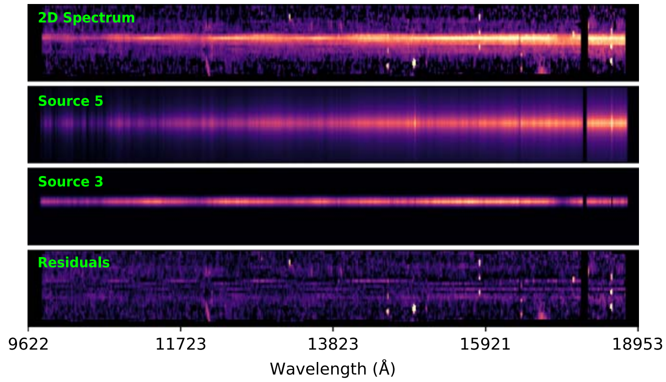

Figure A5. G140M spectrum from Slit B. The top panel shows the 2D spectrum from the JWST pipeline. The middle two panels show the best-fit models of the host galaxy (Source 5) and the SN (Source 3). The bottom panel shows the residuals after subtracting the galaxy and the SN models from the original spectrum.

flux array along the dispersion direction using a median filter with a width of 10 pixels to give a 2D background model. Figure A1 shows an example of the background subtraction.

Subsequently, we extracted spectra of the SN and its host galaxy by fitting extraction kernels simultaneously to the flux in the 2D spectrum as a function of wavelength, as described in

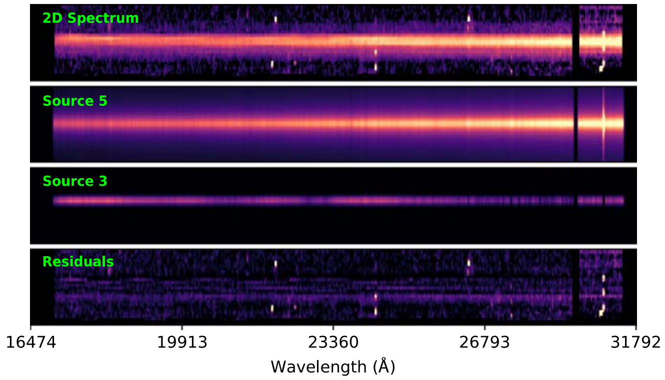

Figure A6. G235M spectrum from Slit B. The top panel shows the 2D spectrum from the JWST pipeline. The middle two panels show the best-fit models of the host galaxy (Source 5) and the SN (Source 3). The bottom panel shows the residuals after subtracting the galaxy and the SN models from the original spectrum.

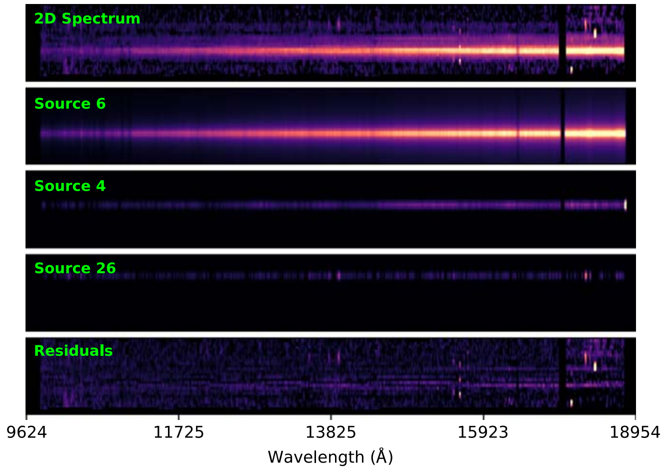

Figure A7. G140M spectrum from Slit C. The top panel shows the 2D spectrum from the JWST pipeline. The middle three panels show the best-fit models of the host galaxy (Source 6), the SN (Source 4), and a nearby arc (Source 26). The bottom panel shows the residuals after subtracting the galaxy and the SN models from the original spectrum.

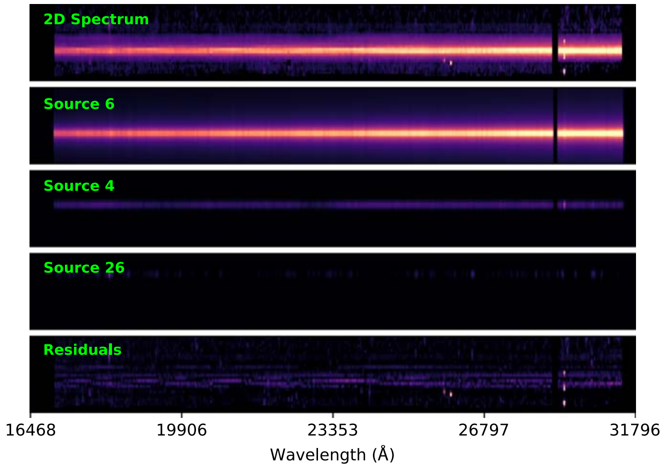

Figure A8. G235M spectrum from Slit C. The top panel shows the 2D spectrum from the JWST pipeline. The middle three panels show the best-fit models of the host galaxy (Source 6), the SN (Source 4), and a nearby arc (Source 26). The bottom panel shows the residuals after subtracting the galaxy and the SN models from the original spectrum.

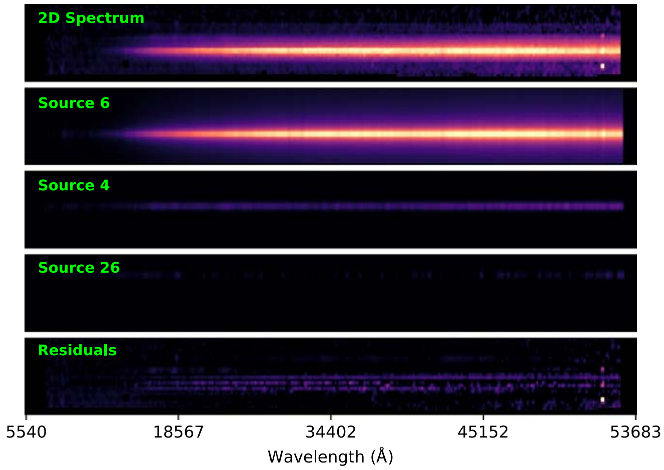

Figure A9. PRISM spectrum from Slit C. The top panel shows the 2D spectrum from the JWST pipeline. The middle three panels show the best-fit models of the host galaxy (Source 6), the SN (Source 4), and a nearby arc (Source 26). The bottom panel shows the residuals after subtracting the galaxy and the SN model from the original spectrum.

Section 2. All the 2D spectra taken from Slits A, B, and C are shown in Figures A2 through A9 (except the NIRSpec PRISM spectra from Slit B, which is shown in Figure 2). Labels are the source names in the MSA configuration data, where SN Images A, B, and C are Sources 2, 3, and 4, respectively, and images of the SN's host galaxy for Images A, B, and C are Sources 6, 7, and 5, respectively.

Appendix B
Results of the Supernova Phase Measurements Before Accounting for Systematic Errors

Table B1 presents the constraints on the phases of the SN images based on the analyses described in Section 5. These constraints arise either from the deviation of the model parameters within the MCMC chains or from the variation in the templates used by the `SNID` software package. The systematic uncertainties derived from our simulations, as described in Section 6, are not included in the error estimates listed in Table B1.

Table B1
SN H0pe Image Phases

	Image A	Image B	Image C
Hsiao (joint)	$52.5^{+11.0}_{-11.4}$	$5.6^{+0.4}_{-0.4}$	$26.0^{+1.0}_{-0.8}$
Hsiao (independent)	$43.4^{+22.2}_{-22.4}$	$5.9^{+0.5}_{-0.6}$	$26.9^{+1.1}_{-1.0}$
SALT3-NIR (joint)	$45.1^{+6.1}_{-8.2}$	$4.2^{+1.1}_{-1.0}$	$27.5^{+0.8}_{-0.7}$
SALT3-NIR (independent)	$36.9^{+7.7}_{-9.0}$	$4.9^{+0.7}_{-1.1}$	$27.8^{+2.2}_{-0.8}$
SNID (templates 2.0)	⋯	$0.5^{+4.2}_{-4.2}$	$25.8^{+13.7}_{-13.7}$
SNID (Ia-norm templates)	⋯	$0.3^{+4.3}_{-4.3}$	$23.3^{+13.3}_{-13.3}$
SNID (SALT3-NIR spectra)	⋯	$5.0^{+6.8}_{-6.8}$	$26.0^{+12.6}_{-12.6}$

Note. Phases are rest-frame days after the peak brightness, and uncertainties are 1σ. For fits with the Hsiao07 templates and the SALT-NIR model, the listed uncertainties encompass solely the dispersion within their respective MCMC samples.

Appendix C
Results from the SALT3-NIR Model

C.1. Joint Markov Chain Monte Carlo Fitting

The primary SALT3-NIR fit was simultaneous to all three images of SN H0pe. Shared parameters comprised the spectral stretch x_1 and color c, as described in Section 5.2. Figure C1 shows the posterior distributions of the fitted parameters. The fits constrain $x_1 = 0.77 \pm 0.23$ and $c = 0.24 \pm 0.02$. Figure C2 illustrates the fit uncertainties. Absorption features at rest-frame ∼4000, ∼4900, and ∼5600 Å in the modeled spectrum at $t = 50$ days (shown in the bottom panel of Figure C2) are likely artifacts due to the model approaching its 50 day phase boundary. No such features have been observed in previous SN Ia spectra.

C.2. Simulation of the Model Fitting

We tested the SALT3-NIR results using simulations similar to those outlined in Section 6. Figure C3 shows inferred versus actual phases for joint fits to a set of nearby SNe Ia. The uncertainties are about the same as those of the Hsiao07 fits for phases $\lesssim 30$ days, and systematic offsets in that range are negligible. At later phases, the inferred phases tend to be a little later than the true phases but consistent with equality within the larger uncertainties.

C.3. Constraints on the Time Delays and Magnifications

We repeated the Section 7 analysis using the SALT3-NIR model, fixing the spectral stretch and color parameters x_1 and c to the best-fit values. The resulting constraints on the phases t_i, magnifications μ_i, and time delays Δt_i are shown in Tables 7 and 8. Values are consistent with those from the Hsiao07 fits within the uncertainties. Calculating absolute magnifications is possible because the luminosities of SNe Ia show small dispersion after correction for light-curve shape and color. For the SALT3-NIR model, we corrected their B-band magnitudes for the spectral stretch (x_1) and color (c) based on the Tripp equation (Tripp 1998), and hence the corrected B-band magnitude ($\hat{m}_B$) is given by $\hat{m}_B = \mu + M = m_B + \alpha x_1 - \beta c$, where μ is the distance modulus, M is the absolute B-band magnitude of a fiducial SN Ia with $x_1 = 0$ and $c = 0$, and m_B is the measured apparent peak magnitude in rest-frame B band. We used $\alpha = 0.15$ and $\beta = 3.0$ from Scolnic et al. (2018) based on the Gaussian intrinsic scatter model of SNe Ia from Guy et al. (2010). Subsequently, comparing $\hat{m}_B$ from peak SALT3-NIR spectra derived from a set of $\boldsymbol{Y}$ parameters from the MCMC chain to the expected $\hat{m}_B$ based on the complete sample from Scolnic et al. (2018) gave the posterior distributions of the magnifications listed in Table 7. An alternative assumption is

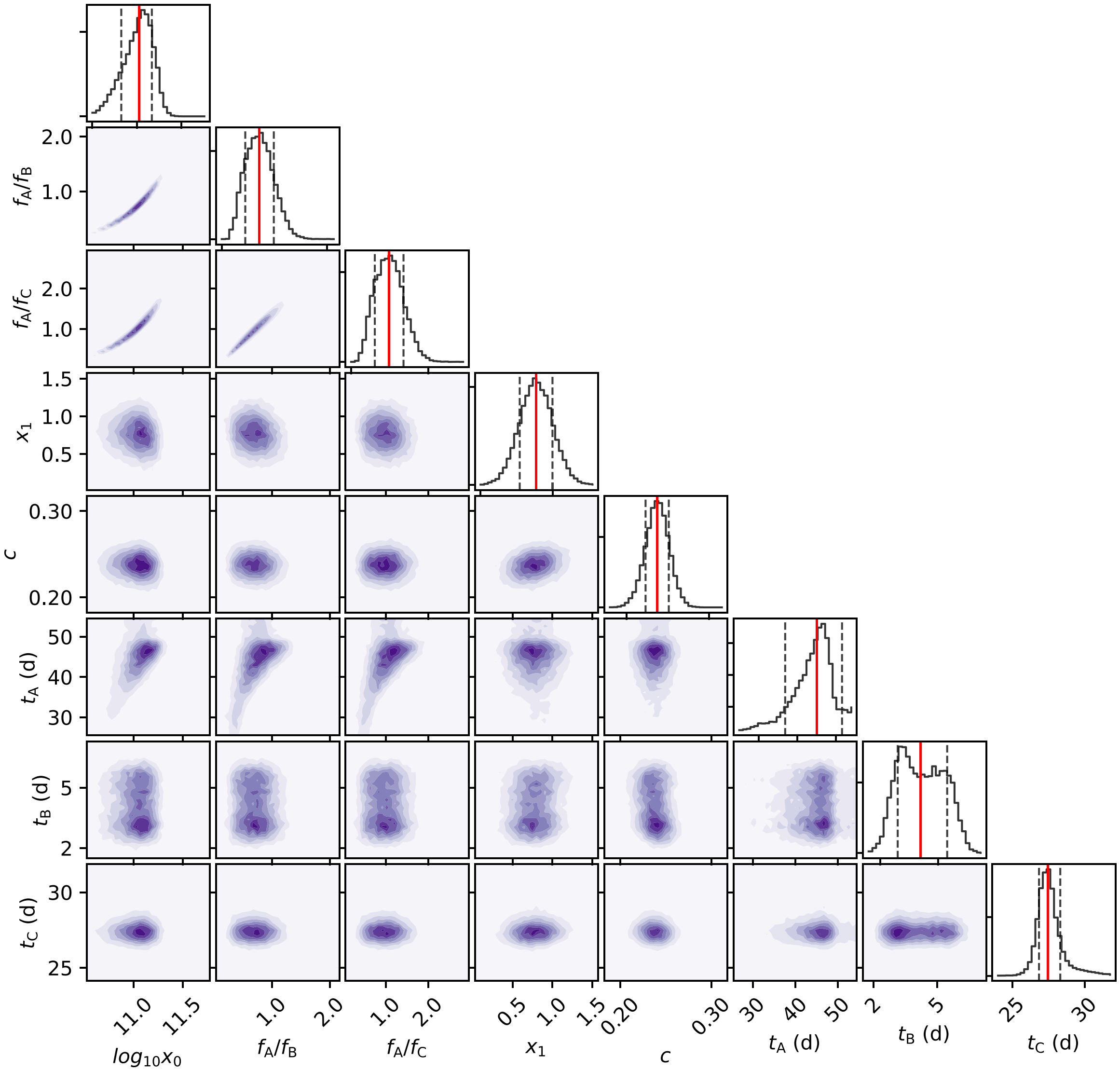

Figure C1. Parameter distributions from the SALT3-NIR model fits. x_0, x_1, and c are the SALT3-NIR model parameters, f_A/f_B and f_A/f_C are the template-flux ratios between Images A and B and between Images A and C, respectively, and t_A, t_B, and t_C are rest-frame phases of Images A, B, and C, respectively. The solid vertical line on each histogram marks the median of the parameter, while the dashed vertical lines denote the 68% confidence interval of each distribution.

that SN H0pe is a standard candle in the rest-frame Y band, as described in Section 7. The Y-band magnitude of a standard SN Ia is characterized by $x_1 = 0$ and $c = 0$ and a rest-frame B-band magnitude equal to the expected $\hat{m}_B$. This gave results consistent with the B-band magnitudes, after applying corrections for spectral stretch and color. The posterior distributions of the SALT3-NIR magnifications are shown in Figure C4, and Table 6 lists the correlation matrices.

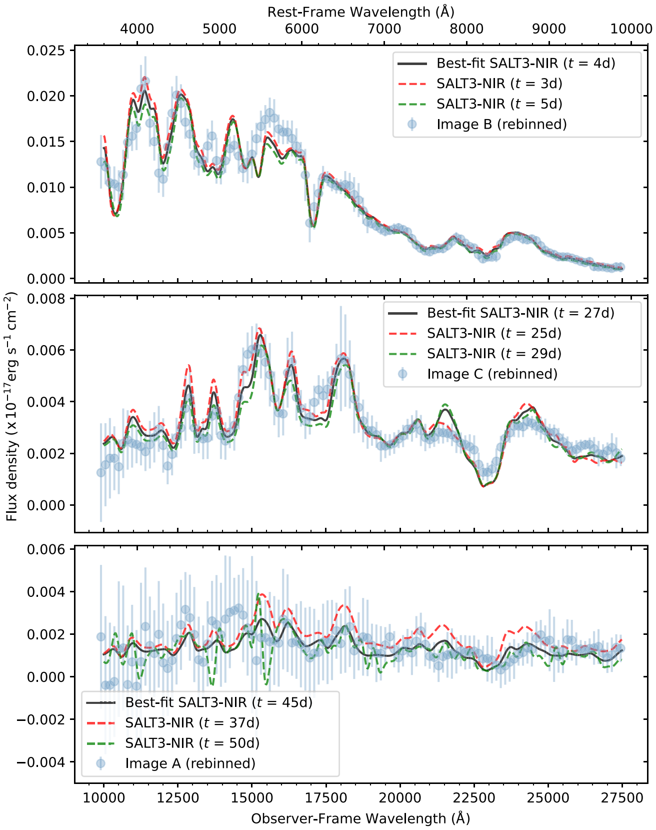

Figure C2. Best-fit SALT3-NIR models from Figure 5 are depicted again here, including the models for SN phases that deviate by $\pm 1\sigma$ (rounded to the nearest integers) from the best-fit phases. Data points and error bars show the observed (120 Å rebinned) SN H0pe spectra.

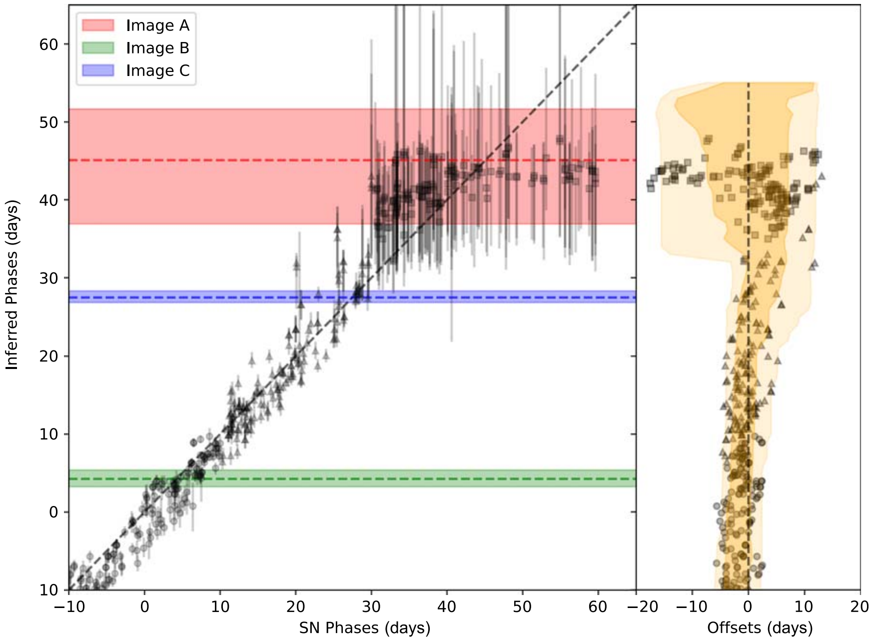

Figure C3. Left: inferred phases from SALT3-NIR fitting vs. actual phases of a set of nearby SNe Ia. Error bars correspond to the 68% confidence intervals of the inferred phases. Horizontal dashed lines and shaded regions mark the inferred phases and their 68% confidence intervals for the three images of SN H0pe. The diagonal dashed line shows equality. Right: deviation of the best-fit inferred phase from the actual phase. Shaded regions mark the 68% (darker) and 95% (lighter) confidence intervals of the residuals measured within a 10 day rolling window. Data points marked by squares, circles, and triangles correspond to spectra with signal-to-noise ratios matching those of Images A, B, and C, respectively.

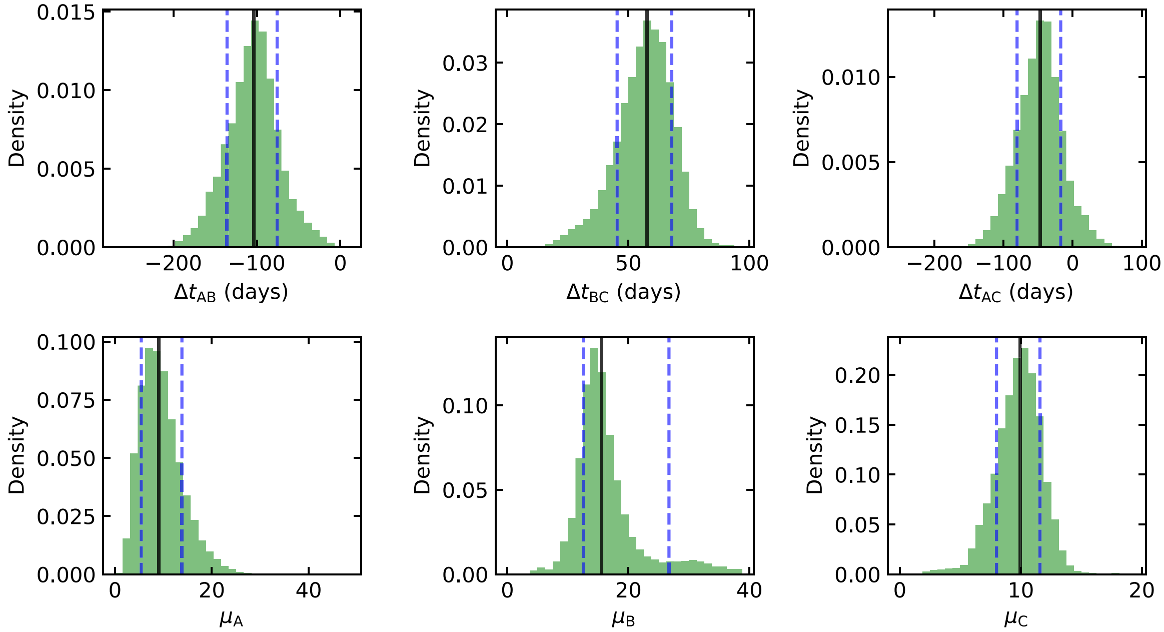

Figure C4. Posterior probability densities of the relative time delays and the macrolens' magnifications between SN H0pe's images. The histograms show the values derived from the SALT3-NIR model. The distributions integrate the uncertainty from the MCMC fitting with systematic uncertainties, estimated from the model fitting of nearby SN Ia spectra and from the simulated SN Ia spectra. The uncertainties take into account the impacts of microlensing and millilensing effects.

ORCID iDs

Wenlei Chen https://orcid.org/0000-0003-1060-0723
Patrick L. Kelly https://orcid.org/0000-0003-3142-997X
Brenda L. Frye https://orcid.org/0000-0003-1625-8009
Justin Pierel https://orcid.org/0000-0002-2361-7201
S. P. Willner https://orcid.org/0000-0002-9895-5758
Massimo Pascale https://orcid.org/0000-0002-2282-8795
Seth H. Cohen https://orcid.org/0000-0003-3329-1337
Christopher J. Conselice https://orcid.org/0000-0003-1949-7638
Lukas J. Furtak https://orcid.org/0000-0001-6278-032X
Daniel Gilman https://orcid.org/0000-0002-5116-7287
Norman A. Grogin https://orcid.org/0000-0001-9440-8872
Simon Huber https://orcid.org/0000-0002-6741-983X
Saurabh W. Jha https://orcid.org/0000-0001-8738-6011
Joel Johansson https://orcid.org/0000-0001-5975-290X
Anton M. Koekemoer https://orcid.org/0000-0002-6610-2048
Conor Larison https://orcid.org/0000-0003-2037-4619
Ashish K. Meena https://orcid.org/0000-0002-7876-4321
Matthew R. Siebert https://orcid.org/0000-0003-2445-3891
Rogier A. Windhorst https://orcid.org/0000-0001-8156-6281
Haojing Yan https://orcid.org/0000-0001-7592-7714
Adi Zitrin https://orcid.org/0000-0002-0350-4488

References

Abbott, T. M. C., Abdalla, F. B., Allam, S., et al. 2018, ApJS, 239, 18
Avelino, A., Friedman, A. S., Mandel, K. S., et al. 2019, ApJ, 887, 106
Barbary, K., Bailey, S., Barentsen, G., et al. 2023, SNCosmo, v2.10.1, Zenodo, doi:10.5281/zenodo.8091892
Blondin, S., & Tonry, J. L. 2007, ApJ, 666, 1024
Bushouse, H., Eisenhamer, J., Dencheva, N., et al. 2023, JWST Calibration Pipeline, v1.10.2, Zenodo, doi:10.5281/zenodo.7829329
Chen, W., Kelly, P. L., Oguri, M., et al. 2022, Natur, 611, 256
Dhawan, S., Johansson, J., Goobar, A., et al. 2020, MNRAS, 491, 2639
Ding, X., Treu, T., Birrer, S., et al. 2021, MNRAS, 503, 1096
Dobler, G., Fassnacht, C. D., Treu, T., et al. 2015, ApJ, 799, 168
Filippenko, A. V. 1997, ARA&A, 35, 309
Foreman-Mackey, D., Hogg, D. W., Lang, D., & Goodman, J. 2013, PASP, 125, 306
Foxley-Marrable, M., Collett, T. E., Vernardos, G., Goldstein, D. A., & Bacon, D. 2018, MNRAS, 478, 5081
Frye, B., Pascale, M., Cohen, S., et al. 2023, TNSAN, 96, 1
Frye, B. L., Pascale, M., Pierel, J., et al. 2024, ApJ, 961, 171
Gilman, D., Birrer, S., Nierenberg, A., et al. 2020, MNRAS, 491, 6077
Goldstein, D. A., Nugent, P. E., Kasen, D. N., & Collett, T. E. 2018, ApJ, 855, 22
Goldwasser, S., Yaron, O., Sass, A., et al. 2022, TNSAN, 191, 1
Goobar, A., Amanullah, R., Kulkarni, S. R., et al. 2017, Sci, 356, 291
Goobar, A., Johansson, J., Schulze, S., et al. 2023, NatAs, 7, 1098
Guy, J., Sullivan, M., Conley, A., et al. 2010, A&A, 523, A7
Horne, K. 1986, PASP, 98, 609
Howell, D. A., Sullivan, M., Perrett, K., et al. 2005, ApJ, 634, 1190
Hsiao, E. Y., Conley, A., Howell, D. A., et al. 2007, ApJ, 663, 1187
Huber, S., Suyu, S. H., Noebauer, U. M., et al. 2019, A&A, 631, A161
Huber, S., Suyu, S. H., Noebauer, U. M., et al. 2021, A&A, 646, A110
Johansson, J., Goobar, A., Price, S. H., et al. 2021, MNRAS, 502, 510
Kelly, P. L., Rodney, S., Treu, T., et al. 2023, Sci, 380, eabh1322
Kelly, P. L., Rodney, S. A., Treu, T., et al. 2015, Sci, 347, 1123
Kelly, P. L., Rodney, S. A., Treu, T., et al. 2016, ApJL, 819, L8
Kenworthy, W. D., Jones, D. O., Dai, M., et al. 2021, ApJ, 923, 265
Moffat, A. F. J. 1969, A&A, 3, 455
Newville, M., Otten, R., Nelson, A., et al. 2021, lmfit/lmfit-py: v1.0.3, Zenodo, doi: 10.5281/zenodo.5570790
Pascale, M., Frye, B. L., Pierel, J. D. R., et al. 2024, arXiv:2403.18902
Pierel, J. D. R., Frye, B. L., Pascale, M., et al. 2024, ApJ, 967, 50
Pierel, J. D. R., Jones, D. O., Kenworthy, W. D., et al. 2022, ApJ, 939, 11
Polletta, M., Nonino, M., Frye, B., et al. 2023, A&A, 675, L4
Refsdal, S. 1964, MNRAS, 128, 307
Riess, A. G., Filippenko, A. V., Leonard, D. C., et al. 1997, AJ, 114, 722
Rodney, S. A., Brammer, G. B., Pierel, J. D. R., et al. 2021, NatAs, 5, 1118
Scolnic, D. M., Jones, D. O., Rest, A., et al. 2018, ApJ, 859, 101
Smith, G. P., Ebeling, H., Limousin, M., et al. 2009, ApJL, 707, L163
Stroe, A., & Savu, V.-N. 2021, AJ, 161, 158
Suyu, S. H., Bonvin, V., Courbin, F., et al. 2017, MNRAS, 468, 2590
Suyu, S. H., Huber, S., Cañameras, R., et al. 2020, A&A, 644, A162
Tonry, J., & Davis, M. 1979, AJ, 84, 1511
Tripp, R. 1998, A&A, 331, 815
Wang, X., Wang, L., Filippenko, A. V., Zhang, T., & Zhao, X. 2013, Sci, 340, 170
Whiting, E. 1968, JQSRT, 8, 1379
Windhorst, R. A., Cohen, S. H., Jansen, R. A., et al. 2023, AJ, 165, 13
Yaron, O., & Gal-Yam, A. 2012, PASP, 124, 668
Zhao, X., Maeda, K., Wang, X., & Sai, H. 2021, MNRAS, 503, 4667